Characterization and diagnostics of corneal transparency by OCT imaging and machine learning

Nuno Miguel Ferreira Vivas Brás
Master in Engineering Physics
Department of Physics and Astronomy
2023

Supervisor
João Manuel Viana Parente Lopes, Assistant Professor
Faculdade de Ciências da Universidade do Porto

Co-supervisor
Karsten Plamann, Lecturer and Researcher
École Polytechnique, ENSTA Paris

Co-supervisor
Anatole Chessel, Lecturer and Researcher
École Polytechnique

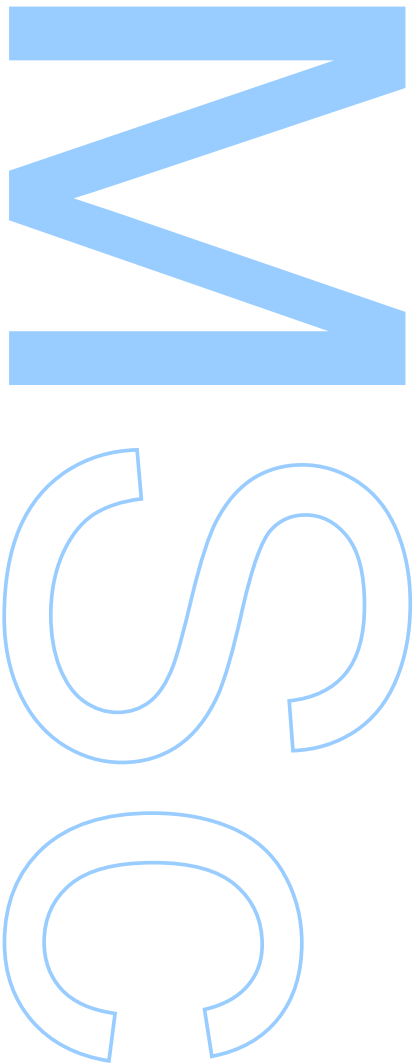

U.PORTO
FACULDADE DE CIÊNCIAS
UNIVERSIDADE DO PORTO
U.PORTO
FEUP FACULDADE DE ENGENHARIA
UNIVERSIDADE DO PORTO

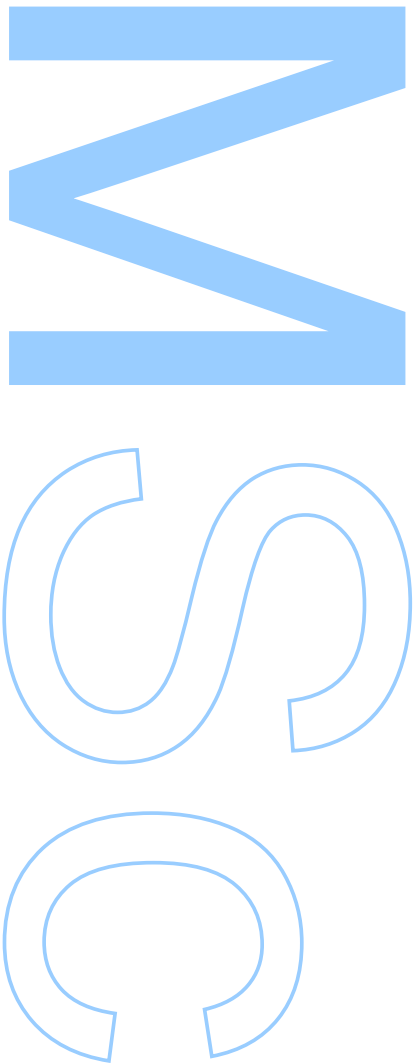

Acknowledgments

I sincerely thank those who have been instrumental in my academic journey. I am grateful for the collective contributions of my mentors and colleagues, who have shaped this thesis. To my supervisor at FCUP, João Viana Lopes, I extend my heartfelt thanks. His weekly guidance and assistance in navigating challenges have been invaluable. I am deeply thankful to my supervisors at LOB, Karsten Plamann and Anatole Chessel, for allowing me to work with them during this thesis. Their complementary expertise has enriched my knowledge and opened doors to future research, including a PhD.

I also want to acknowledge the entire LOB laboratory for welcoming me and offering an environment conducive to learning and research.

Resumo

A córnea humana, responsável por dois terços do poder óptico do olho, depende de estruturas micro e nanométricas para manter a transparência. No entanto, várias patologias podem perturbar esse delicado equilíbrio, reduzindo a transparência e causando deficiências visuais. A perda de transparência da córnea é uma das principais causas de cegueira em todo o mundo, exigindo detecção e intervenção precoces.

Esta tese é parte de um projeto de pesquisa colaborativa entre o Laboratoire d'Optique et de Biosciences (LOB ; École Polytechnique / CNRS / INSERM) e o Hospital Quinze-Vingts em Paris. Utilizamos técnicas de análise de imagens de córneas saudáveis obtidas por tomografia de coerência óptica e conduzimos uma análise preliminar da estrutura da córnea. Conseguimos destacar certas vantagens dos métodos baseados em inteligência artificial em comparação com os métodos de segmentação convencionais na análise da córnea com o objetivo de melhorar o diagnóstico precoce e o tratamento, aprimorando assim o cuidado ao paciente.

Pesquisas futuras devem investigar a dispersão em ângulos elevados (>1º) e transferir essa técnica para imagens "in vivo" de alta resolução e, posteriormente, para dados clínicos de baixa resolução. O objetivo final é traduzir essas descobertas em ferramentas clínicas de fácil utilização, abordando uma genuína necessidade de saúde pública.

Palavras-chave: Transparência da Córnea, Tomografia de Coerência Óptica, Aprendizagem Profunda, Óptica Biomédica, Visão Computacional, Imagens de Alta Resolução

Abstract

The human cornea, responsible for two-thirds of the eye's optical power, relies on precise micro- and nano-scale structures to maintain transparency. However, various pathologies can disrupt this delicate balance, reducing transparency and causing visual impairments. Corneal transparency loss is a leading cause of blindness worldwide, necessitating early detection and intervention.

This thesis is part of a collaborative research project between the Laboratoire d'Optique et de Biosciences (LOB ; École Polytechnique / CNRS / INSERM) and Quinze-Vingts Hospital in Paris. We utilized image analysis techniques of healthy corneas obtained through optical coherence tomography and conducted a preliminary analysis of corneal structure. We were able to highlight certain advantages of artificial intelligence-based methods compared to conventional segmentation methods in corneal analysis for the purpose of improving early diagnosis and treatment, ultimately enhancing patient care.

Future research should investigate high-angle (>1º) scattering and the transfer of the method to high-resolution in vivo images, followed by low-resolution clinical data. Ultimately translating these findings into user-friendly clinical tools, addressing a genuine public health need.

Keywords: Corneal Transparency, Optical Coherence Tomography (OCT), Deep Learning, Biomedical Optics, Computer Vision, High-Resolution Imaging

Résumé

La cornée humaine, responsable de deux tiers de la puissance optique de l'œil, est transparente dans son état sain à cause de ses structures très régulières aux échelles micrométriques et nanométriques. Cependant, diverses pathologies peuvent perturber cet équilibre délicat, réduisant la transparence et provoquant des troubles visuels. La perte de transparence de la cornée est l'une des principales causes de cécité dans le monde, nécessitant une détection précoce et pour pouvoir procéder à une intervention.

Le présent projet de master s'inscrit dans un projet de recherche collaboratif entre le Laboratoire d'Optique et de Biosciences (LOB ; École Polytechnique / CNRS / INSERM) et l'Hôpital Quinze-Vingts à Paris. Nous avons utilisé des techniques d'analyse d'images de cornée saines obtenues par tomographie par cohérence optique et nous avons procéder à une analyse préliminaire de la structure cornéenne. Nous avons pu mettre e évidence certains avantages de méthodes s'appuyant sur l'intelligence artificielle par rapport aux méthodes de segmentation conventionnelles dans l'analyse de la cornée en vue d'une amélioration du diagnostic précoce et leur traite ment, afin d'améliorer le suivi des patients.

Les futures recherches devraient examiner la diffusion à haut angle (>1º) et le transfert de la méthode vers des images in vivo à haute résolution, puis des données cliniques à basse résolution. L'objectif ultime sera le transfert de notre technique vers la routine clinique, ainsi répondant à un vrai besoin de santé publique.

Mots-clés: Transparence cornéenne, Tomographie par cohérence optique, Apprentissage profond, Optique biomédicale, Vision par ordinateur, Imagerie haute résolution

Contents

List of Tables

List of Figures

Introduction

he human cornea, responsible for two-thirds of the eye's optical power, is a connective tissue with a regular organisation of structures at the micrometre and nanometer levels, ensuring transparency. However, specific pathologies can disrupt the collagen structure and give rise to diffusing structures within the cornea, resulting in a loss of transparency. Depending on their size and distribution, these diffusing structures can significantly impact visual acuity and contrast sensitivity, leading to potential glare-related issues. The loss of corneal transparency is a prevalent cause of blindness, affecting over 10 million individuals worldwide. Many underlying conditions can contribute to this transparency loss, some of which may necessitate a complete corneal transplant. However, early detection of these conditions could prevent the need for such invasive procedures. Moreover, the scarcity of corneal grafts in numerous countries highlights the importance of enhancing diagnosis and treatment methods to reduce reliance on transplantation. Early diagnosis and quantitative monitoring can improve clinical outcomes and mitigate the global burden of blindness. Additionally, a reliable and quantitative measurement of corneal transparency can provide valuable prognostic information following transplantation. Thus, developing user-friendly and objective clinical tools for accurately characterising corneal transparency is paramount.

The collaborative research project between the Laboratoire d'Optique et de Biosciences (LOB ; École Polytechnique / CNRS / INSERM) and Quinze-Vingts Hospital in Paris aims to study cornea's transparency in vitro and in vivo by employing new developments in deep learning methodologies to determine the number, extent, and optical contrast of diffusing objects within the corneal tissue. By understanding the distribution of diffusing structures, we aim to predict the angular distribution of the scattering pattern, which directly affects contrast sensitivity and glare phenomena in patients with corneal disorders. This knowledge will aid in postoperative follow-up after corneal transplantation and contribute to diagnosing ocular conditions such as Fuchs dystrophy. To achieve this, we rely on high-resolution optical coherence tomography (OCT) imaging of corneal samples in vitro and clinical devices for in vivo imaging.

The project is currently in its third phase (Figure 1). It started with developing a new physical model describing light propagation in the cornea, explicitly focusing on corneal diffusers [2]. Following this, an analysis methodology for quantitatively assessing corneal

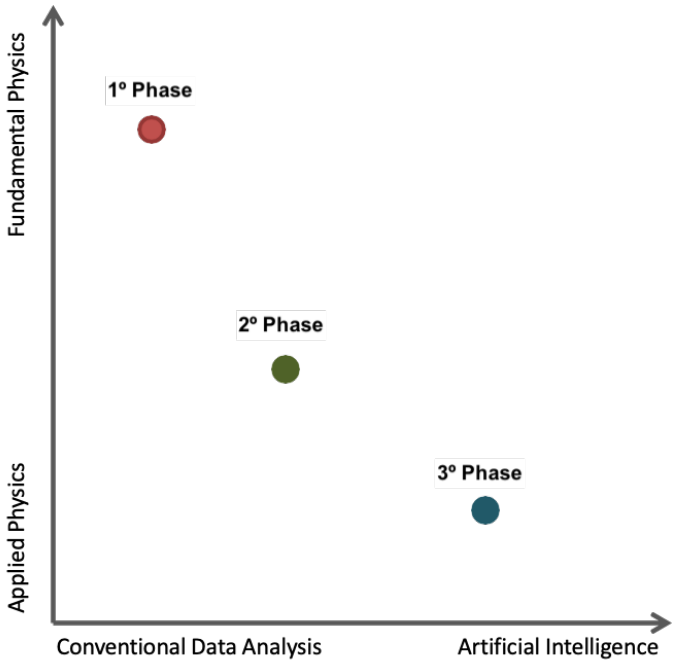

Figure 1: Research Project - Work Plan

transparency was developed and validated in vivo using optical coherence tomography (FF-OCT) [23]. The current phase aims to study the influence of keratocytes, cells that sparsely populate the corneal stroma and significantly contribute to its transparency. The goal is to construct a model for analysing and characterising keratocytes' structural properties using artificial intelligence. The primary objective is to define clinically relevant parameters to evaluate corneal conditions and facilitate patient follow-up. This phase bridges the gap between theoretical concepts and practical clinical applications.

This thesis plays a necessary preliminary result in choosing the most efficient image analysis techniques and early characterisation parameters for future model stabilisation of corneal structure assessment, offering a valuable set of results and conclusions that will guide our selection of corneal analysis methods. Only healthy corneas from high-resolution OCT were studied during the six months of work, establishing an essential benchmark for comparative analysis in future studies involving corneas with pathological conditions. The following chapters will elucidate the work done in segmentation methodologies to identify keratocytes in the cornea and measure these objects' influence on the cornea's general transparency by doing typical Fourier analysis in the field, such as Point spread function, Strehl ratio and visual acuity.

Chapter 1

Human Cornea

1.1 Eye - Optical System

1.1.1 Anatomy of the Eye

The human eye functions as the initial point of light entry and comprises several optical elements that give its refractive power. The cornea, approximately 0.55 mm thick at the centre, with slightly increasing thickness towards the periphery, is the eye's first lens, responsible for about two-thirds of its optical power and protecting the external environment. The remaining third is provided by the crystalline lens, a deformable lens enabling accommodation. These two lenses allow the passage and focusing of light onto the retina — a light-sensitive membrane positioned at the rear of the eye. The retina converts light into neural signals through the activity of specialized photoreceptor cells known as rods and cones. These cells detect photons and initiate neural impulses in response. The resulting signals are then conveyed via the optic nerve, transmitting information from the retina to the central ganglia of the brain, including the lateral geniculate nucleus, which further relays it to the visual cortex. The human visual system exhibits sensitivity to visible light within the wavelength range of 380 to 730 nanometers within the electromagnetic spectrum. The resolution power of an emmetropic eye, meaning it has no refractive errors, is approximately one minute of arc. Similar to classical optical systems, the pupil's size affects the resolution. For a small-sized pupil (2 to 3 mm), the resolution is limited by diffraction, while for larger pupils, aberrations will limit resolution (peaking at 8 mm). The maximum resolution is generally observed for an intermediate pupil size (3 to 4 mm) [8].

From an optical design perspective, the eye differs significantly from imaging systems engineered in optical engineering, making it challenging to optimize refractive correction surgeries. Figure 1.1 illustrates the different axes of the eye's optical elements.

The optical axis is the line connecting the centres of curvature of the refractive elements in a centred optical system. Since the eye is not centred, it does not have a true optical axis, but one can define an axis corresponding to the linear fit of the centres of

curvature of the spheres fitted to the cornea and the lens surfaces.

The visual axis is the line connecting the fixation point, nodal points, and the fovea (the region of precise vision). The nodal points are two points on the optical axis that conjugate with each other, where an incoming ray through the first point exits through the second point with an angle equal to the angle of incidence with respect to the optical axis.

The line of sight connects the fixation point and the centre of the entrance pupil. This line is not fixed as the centre of the pupil moves depending on the pupil's aperture.

The pupillary axis is the line passing through the centre of the pupil and perpendicular to the corneal surface. Since the pupil is often decentered with respect to the cornea, the pupillary and optical axes are not coincident.

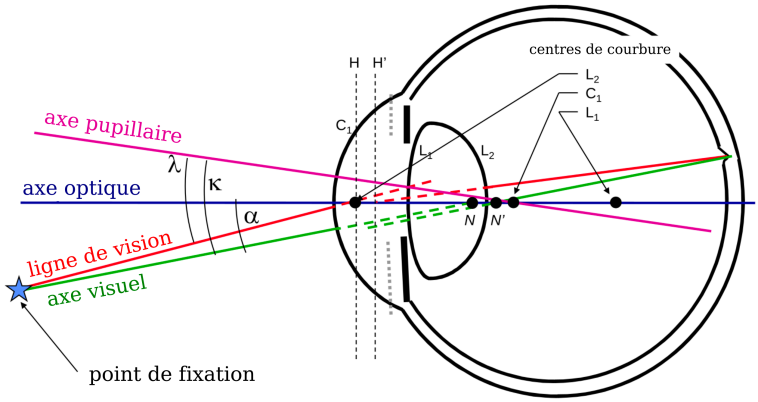

Figure 1.1: Eye Axis. Taken from [2]

1.1.2 Vision Domain

The retina has two types of photoreceptor cells responsible for phototransduction:

- **the cones** exist in three types, allowing trichromatic vision in photopic conditions (daylight). A dense hexagonal mosaic of cones in the central zone of the retina, the fovus, is at the origin of the perception of details in the central zone of the visual field, which is the area of attention of the subject
- **the rods**, absent from the foveal region, are more sensitive to light than the cones. They condition low luminance vision (scotopic vision). There is not only one type of rod, so the night vision is monochromatic.

The eye is sensitive to light over a wide range of luminance levels. The eye's dynamic range varies on a logarithmic scale, covering approximately 15 orders of magnitude (from the sensitivity limit of rods, the most sensitive photoreceptors, to direct sun observation).

The maximum level of resolution in the human eye is attained within the central region known as the fovea. At the center of the fovea, the angular resolution limit decreases to approximately 30 seconds of arc, equivalent to perceiving a spatial period of 0.1 mm

when viewed from a distance of 1 meter. In clinical settings, this maximum resolution is evaluated through visual acuity assessments, which are commonly expressed on a decimal scale (with 10/10 representing maximum visual acuity) or in logMAR units (where MAR denotes the minimum angle of resolution, and a visual acuity of 0.0 logMAR signifies maximum acuity). Beyond the foveal region lies the peripheral vision area. In this region, the eye is more responsive to motion and contrasts at lower spatial frequencies [20].

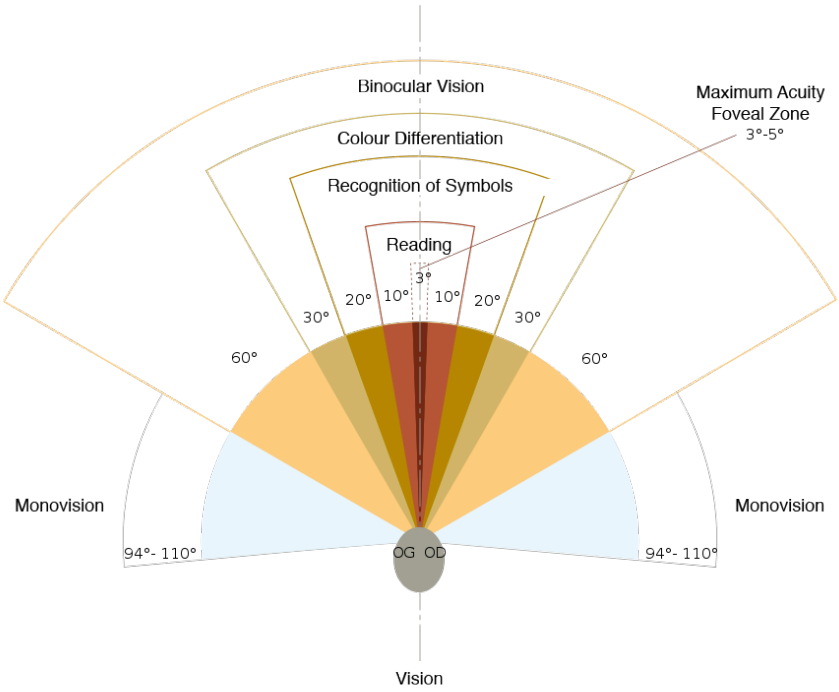

Figure 1.2: Human visual field. Taken from [23]

1.2 Structure of Cornea

The cornea is a transparent structure located at the front of the eye. It serves as a protective covering (encompasses the pupil and the iris) and is responsible for focusing most of the light that enters the eye. The cornea, composed of proteins and cells, distinguishes itself by lacking blood vessels, unlike most human tissues. The absence of blood vessels helps maintain the cornea's transparency, enabling proper refraction of light and preserving optimal vision. To compensate for the absence of blood vessels, the cornea receives nutrients from tears and the aqueous humor (a watery fluid) in the anterior chamber.

1.2.1 Histology of the cornea

The human cornea comprises five highly specialized layers, each with its specific structure and function.

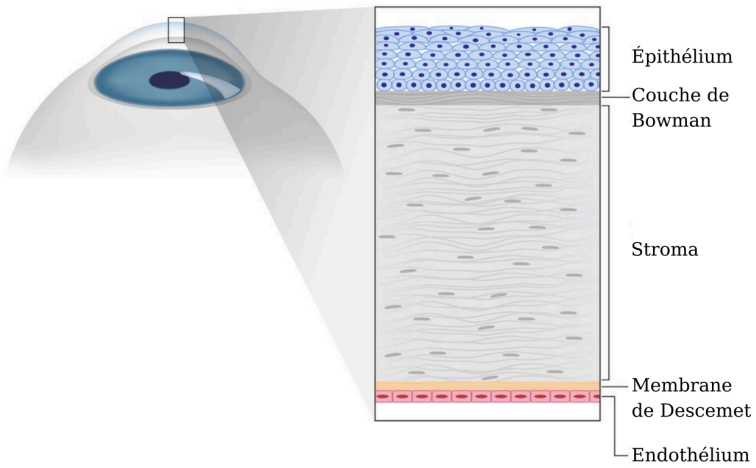

Figure 1.3: Structure of Cornea. Taken from [2]

- **Epithelium:** a fast-growing and regenerating multi-cellular layer, is the most superficial layer of the cornea. It has a structure comprising 5 to 7 layers of superposed cells and a total thickness of approximately 50 to 52 μm. Its cells are shed constantly on the exposed layer and are regenerated by multiplication in the basal layer. Any irregularity of the corneal epithelium disrupts the smoothness of the air/tear-film interface, contributing to decreased visual acuity.
- **Bowman's layer:** an acellular layer between the corneal epithelial basal membrane and the corneal stroma. Composed of disorganized collagen fibers, it has a thickness between 10 μm to 20 μm.
- **Stroma:** the most extensive layer of the cornea and makes up approximately 90% of its thickness. It provides unique properties necessary for function, including transparency and avascularity, as well as its mechanical properties necessary for strength and shape maintenance. It has collagen fibers arranged in a regular pattern along with sparsely distributed interconnected keratocytes, which are the cells for general repair and maintenance. These lattice arrangements of the collagen fibrils in the stroma dictate the cornea transparency and will be discussed more in-depth in the upcoming sections.
- **Descemet's membrane:** an acellular layer made of collagen fibrils and fibronectin that allows the adhésion to the stroma. It has a thickness of about 3 μm to 4 μm at birth and 10 μm to 12 μm during adult life.
- **Endothelium:** a single layer of either simple squamous or cuboidal cells that do not proliferate. Instead, they stretch to compensate for dead cells, reducing the endothelium's overall cell density. These cells are responsible for maintaining fluid balance and preventing swelling of the stroma through sodium pumps in their membranes. If the endothelium can no longer maintain a proper fluid balance, stromal swelling due to excess fluids and subsequent loss of transparency will occur, and

this may cause corneal edema and interference with the transparency of the cornea, thus impairing the image formed.

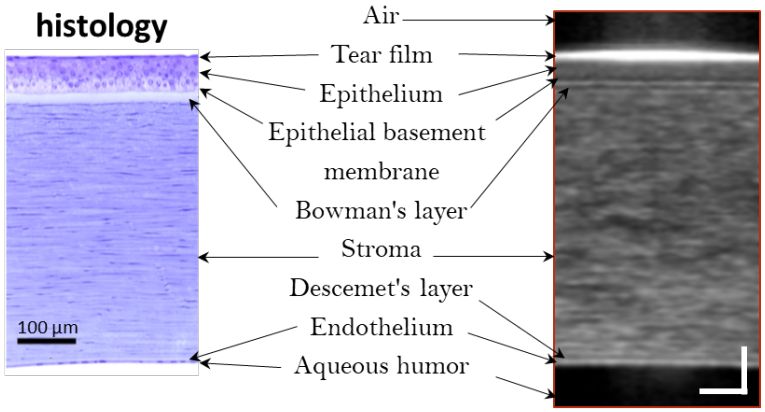

Figure 1.4: Histology of Cornea. Taken from [23]

1.2.2 Collagen Structure

Corneal collagen has several crucial properties as the primary structural component within the tissue. The collagen fibrils are uniform in diameter, narrow, and precisely organized, essential for maintaining transparency and providing the necessary biomechanical properties to sustain the cornea's shape and strength. The stroma consists of collagen lamellae that vary in thickness and are interwoven in the anterior region, while the posterior lamellae are more hydrated and arranged in a plywood-like fashion. The central cornea typically contains around 200 lamellae. The lamellar arrangement in the cornea is essential for maintaining its overall shape and specific optical properties, such as corneal birefringence. However, transparency is primarily determined by the absence of scatter-inducing structures, such as keratocytes, and by the structural organization of collagen fibrils within the lamellae.

The structural hierarchy of corneal collagen involves coiling three helical alpha chains to form a collagen triple helix molecule. These molecules then assemble in a staggered axial array to form microfibrils consisting of five molecules. The microfibrils further coil together to create the 30 nm diameter collagen fibrils.

Corneal collagen fibrils serve as the primary load-bearing components of the lamellae in the cornea. They must withstand the tensile forces resulting from intraocular pressure and protect the inner ocular tissues from external trauma while maintaining their narrow size for tissue transparency.

1.2.3 Keratocytes

Keratocytes (fig.1.6) are quiescent cells originating from neural crest cells situated between the collagen lamellae. Even though the collagen structures heavily influence the

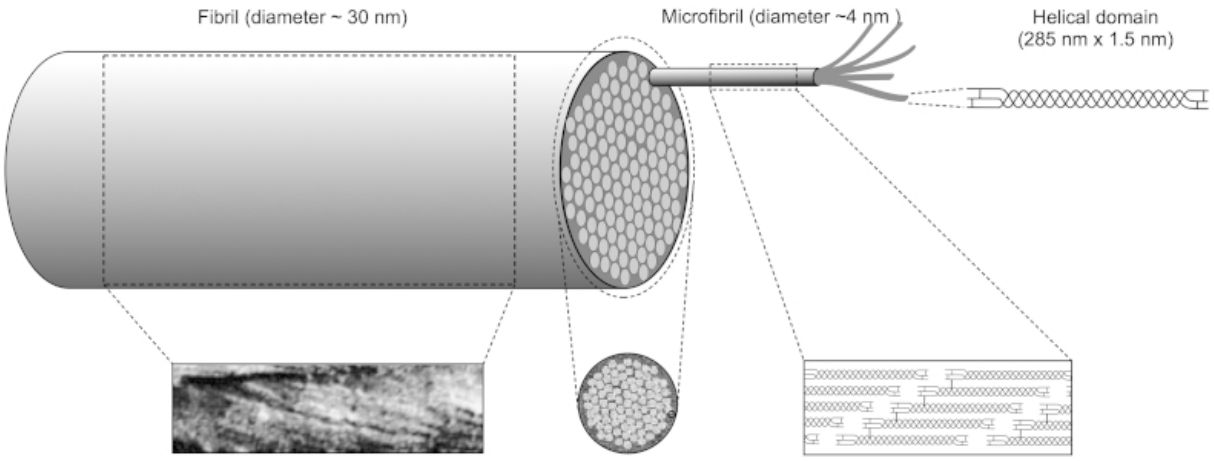

Figure 1.5: Structural hierarchy in corneal collagen. Three helical alpha chains are supercoiled to produce the collagen triple helix molecule (top right). These molecules self-assemble in a staggered axial array (bottom right) to form microfibrils consisting of five molecules that turn coil together to form the 30 nm diameter collagen fibrils seen in the electron microscope. The graph in the bottom left shows the coiled microfibrils within the collagen fibril; the graph in the bottom middle shows the microfibrils in cross-section within the collagen fibril. Taken from [14]

cornea's transparency, the keratocytes also have a role in this phenomenon. Their main functions are:

- maintains the stroma's collagen structure and extracellular matrix by synthesizing collagen molecules, proteoglycans, and matrix metalloproteinases.
- clearance of cellular debris and waste products from the cornea. This process is essential for preventing the accumulation of materials that could interfere with corneal transparency.

Since they occupy a small percentage of the volume of the stroma (<10%), the total light scattered is small. However, these cells can be activated after injury, leading to an increase of scatterer cells in the stroma.

1.2.4 Refraction of cornea

Corneal refraction relies on its two aspherical and convex-like surfaces. The curvature radius of these surfaces increases as it move away from the corneal apex, also known as the center of the cornea. However, we can determine the radii of curvature (R) of the central cornea within a 3 mm diameter. On average, the anterior face has a radius of curvature of ($C1_{95}$: 7.3-8.3 mm), while the posterior surface has a radius of curvature of ($C1_{95}$: 6.0-7.0 mm) [1]. Considering the refractive indices (n) on both sides of the interfaces, we can measure the associated refractive powers (P), denoted as $P = \Delta n/R$.

In the 20th century, the widely accepted corneal refractive index was 1.376, proposed in Gullstrand's model of the eye, for which he was awarded the Nobel Prize in Physiology in 1911 [9]. However, a single index cannot account for light backscatter observed

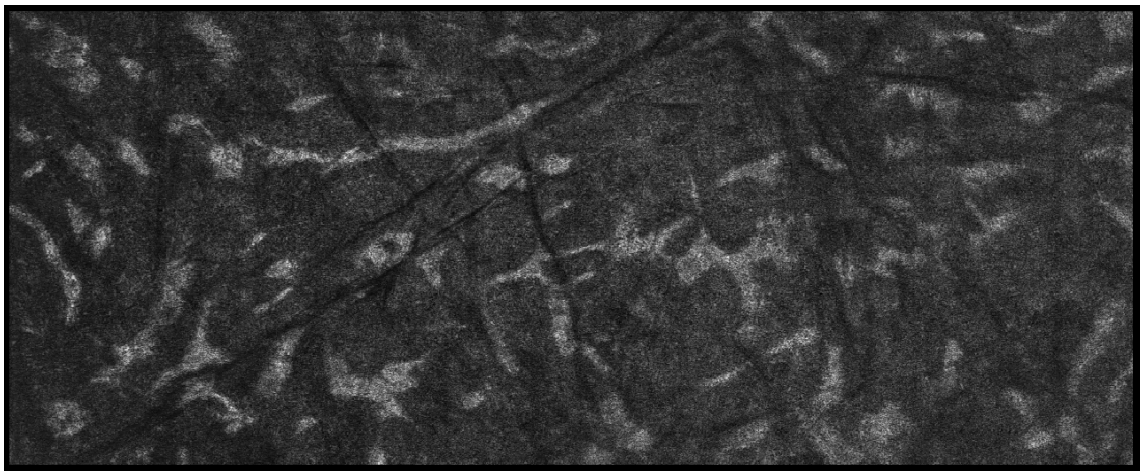

Figure 1.6: Plane image of a fraction of the corneal stroma obtained by Optical Coherence Tomography. The white regions represent the keratocytes.

in the cornea or accommodate the heterogeneity of this tissue, as well as the biological variability between healthy and pathological corneas [15]. In addition, accurately calculating refractive parameters for corneal refractive surgery or cataract surgery, aiming to minimize ”post-operative refractive surprises,” necessitates precisely determining corneal refractive indices in vivo. To address the lack of measurements on the posterior surface of the cornea, a reduced refractive index known as the ”keratometric index” is employed in these calculations [7].

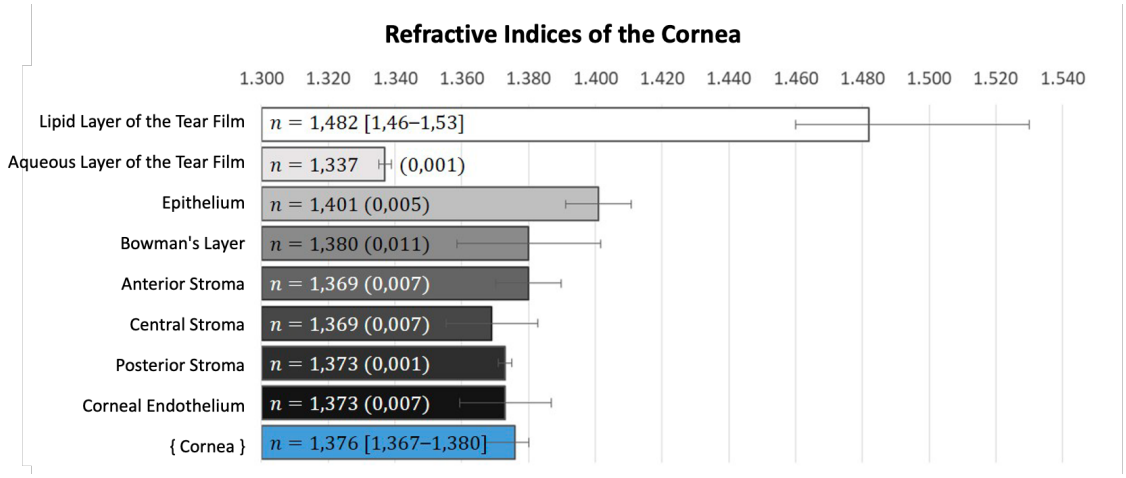

Figure 1.7: Refractive Indices of Different Corneal Layers. Taken from [23]

1.3 Transparency of the Cornea

1.3.1 Origin of Corneal Transparency

The transparency of the corneal stroma has intrigued researchers since the nineteenth century. Initially, it was believed that a uniform composition was necessary for corneal transparency. However, discovering a significant difference in refractive index between

the collagen fibrils and the interstitial matrix challenged this notion. Alternative mechanisms were proposed, such as the interference of scattered light waves from ordered crystalline arrays of collagen fibrils. In this section, it will be provided an overview of the current understanding of corneal transparency.

The interaction of electromagnetic waves with scattering structures generates the emission of secondary spherical waves. The superposition of these secondary waves creates cylindrical waves propagating radially away from the fibril. The intensity and propagation of these waves are influenced by factors such as the radius of the collagen fibril, refractive index inside and outside the fibril, wavelength and polarization of the incoming electromagnetic field, and direction of propagation of the secondary waves. Collagen fibrils act as scatterers, transferring a portion of the energy from incoming waves to secondary waves scattered in all directions. Very little incoming light would reach the retina without interference, resulting in opacity. For this problem, Maurice proposed that the secondary waves interfere with each other, cancelling out in most directions except the forward direction. This interference phenomenon transfers energy from incoming to secondary waves that successfully pass through the cornea.

Corneal transparency is then a complex phenomenon that relies on the structure and organization of collagen fibrils within the extracellular matrix. The organization of collagen fibrils is crucial for this phenomenon since the random distribution of the fibrils would lead to opacity due to heavy scattering. David Maurice (1957) [13] proposed that the collagen fibrils must be organized regularly to allow constructive interference in the direction of light propagation. This paper delves into the various factors influencing corneal transparency, including the arrangement of collagen fibrils, the impact of fibril diameter variations, the role of hydration and gel pressure, and the significance of short-range order in the extracellular matrix. This paper suggested that a perfect hexagonal lattice of collagen fibrils, with a constrained distance between adjacent fibrils (a fraction of the wavelength of the incoming wave), facilitates constructive interference and transparency. However, the requirement of a perfect hexagonal lattice is flexible as long as the distance between adjacent fibrils is constrained.

Figure 1.8 shows the secondary radiation emerging from an arrangement of fibrils whose positions are random but with a restriction of the distance between two fibrils no smaller than 62 nm (distance at which two fibrils would touch). In this case, only the forward radiation may be present since the backward radiation was cancelled entirely.

A decrease in corneal transparency can occur when some adjacent fibrils fuse, generating backward scattering. Figure 1.9 represents this type of situation. Here, the arrangement of fibrils has the same conditions as Fig.1.8 but with 20% of the fibrils having a diameter twice the normal. This difference is enough to create backward scattering due to the difference in amplitude of the secondary waves created, preventing destructive interference.

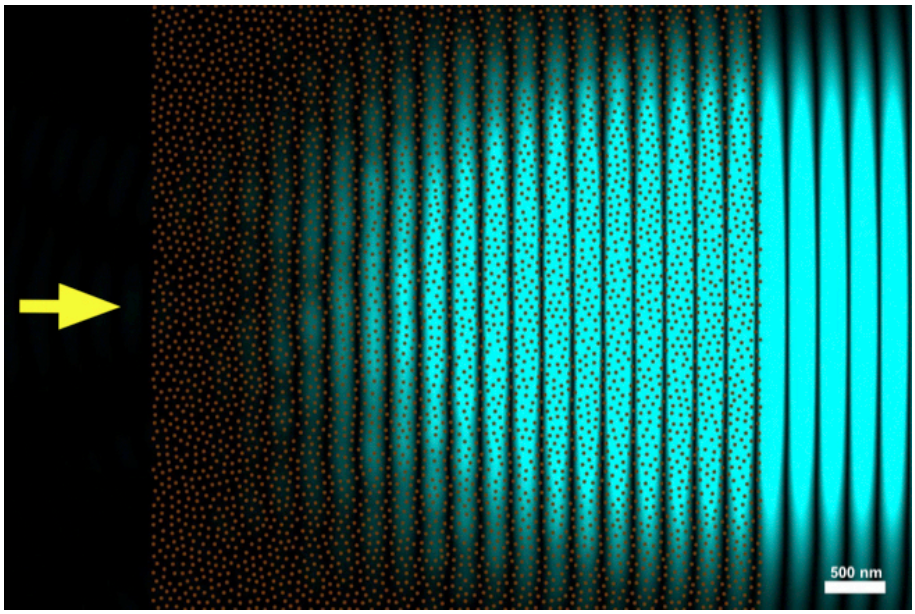

Figure 1.8: Secondary waves from a collagen fibril distribution presenting short-range order. Primary incoming light travels from left to right (yellow arrow) with a wavelength of 500 nm. Brown circles represent collagen fibrils in transverse sections. All fibrils have the same diameter of about 31 nm, and no collagen fibrils can be closer than 62 nm. Only the intensity of the secondary radiation arising from the fibrils is shown in blue. No backwards secondary radiation can be seen in the figure. Taken from [14]

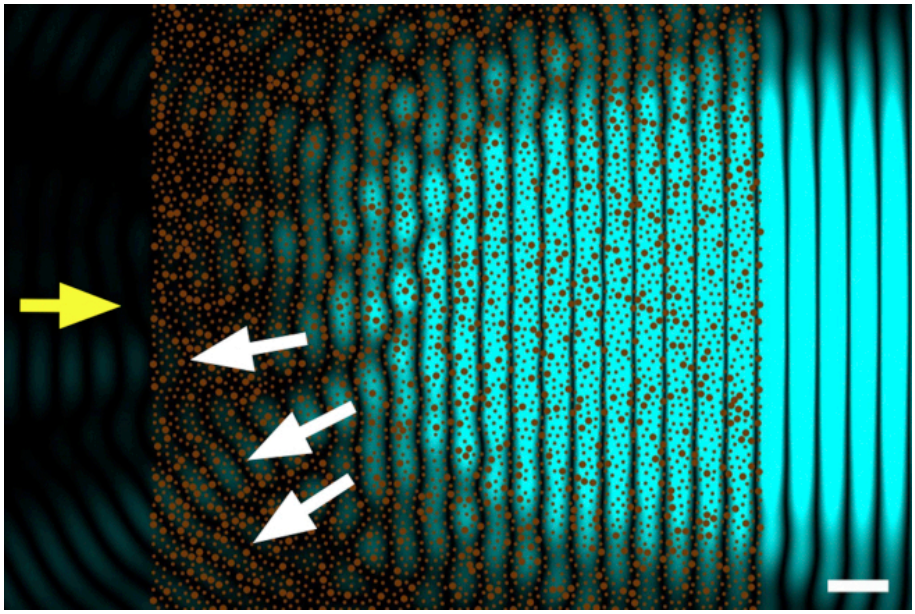

Figure 1.9: The effect of increased fibril diameters on light transmission. 20% of the fibrils were selected at random, and their diameter was doubled to 62 nm. The intensity of the secondary radiation arising from the fibrils is shown in blue. Backwards secondary radiation is evident in the figure (white arrows). Taken from [14]

Figure 1.10 represents the particular case of voids in the collagen structure. This can happen when the cornea swells, increasing the quantity of scattered light and contributing to a loss of transparency. The structure conditions are equivalent to the ones in fig.1.8 with

the addition of structural gaps. Backscattered light arises from this mechanism because the missing fibrils can no longer cancel the secondary radiation. It is worth noting that the

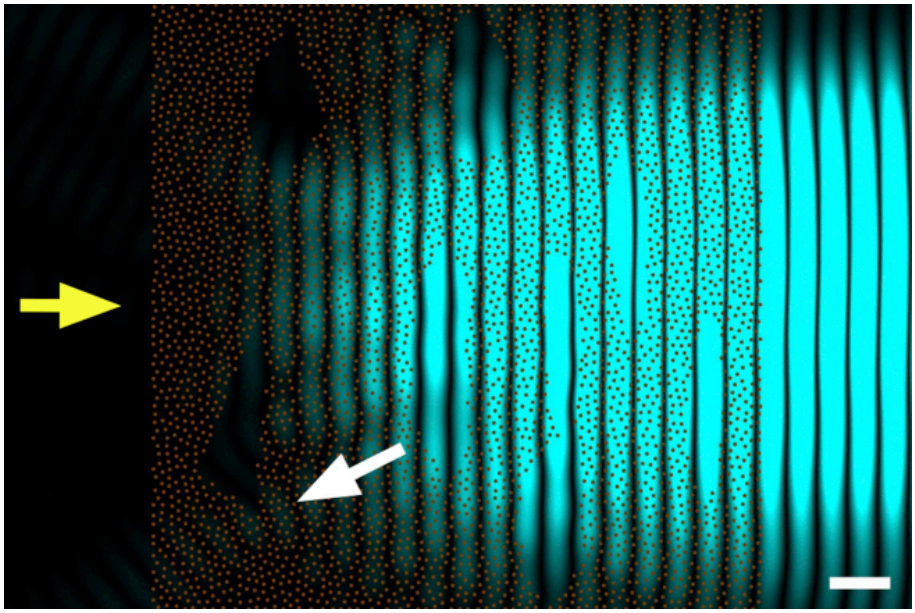

Figure 1.10: The effect of fibril voids on light transmission. Regions devoid of fibrils are now present (lakes). The intensity of the secondary radiation arising from the fibrils is shown in blue. Even in this case, backwards secondary radiation is evident in the figure (white arrow). Taken from [14]

situations presented above only consider a small region of collagen. In a real situation, we have much more fibrils, so in cases with backscattered light, the loss of intensity in the direction of the retina is greater.[14]

A more mathematical approach for this question is to use Fourier optics (Fig.1.11). The squared magnitude of the Fourier transform of the fibril distribution relates to the scattered power, while the Fourier transform of the autocorrelation function describes the organization of fibrils. The interfibrillar distance and its variation affect the diffraction pattern and angular distribution of scattered power, leading to forward or backward scattering.

1.3.2 Light Scattering by the cornea

There are two main scattering regimes to consider: Rayleigh and Mie scattering. Rayleigh scattering occurs when the size of the scattering structures (such as collagen fibrils) is much smaller than the wavelength of light. In this regime, the scattered light is predominantly directed forward, resulting in minimal visual disturbance. Mie scattering, on the other hand, occurs when the size of the scatterers is comparable to or larger than the wavelength of light. Mie scattering can cause light to scatter in various directions, leading to a broader range of angles and potentially reducing corneal transparency.

In the cornea, the collagen fibrils can be considered Rayleigh scatterers, which scatter light predominantly in the forward direction. However, suppose the organization of the

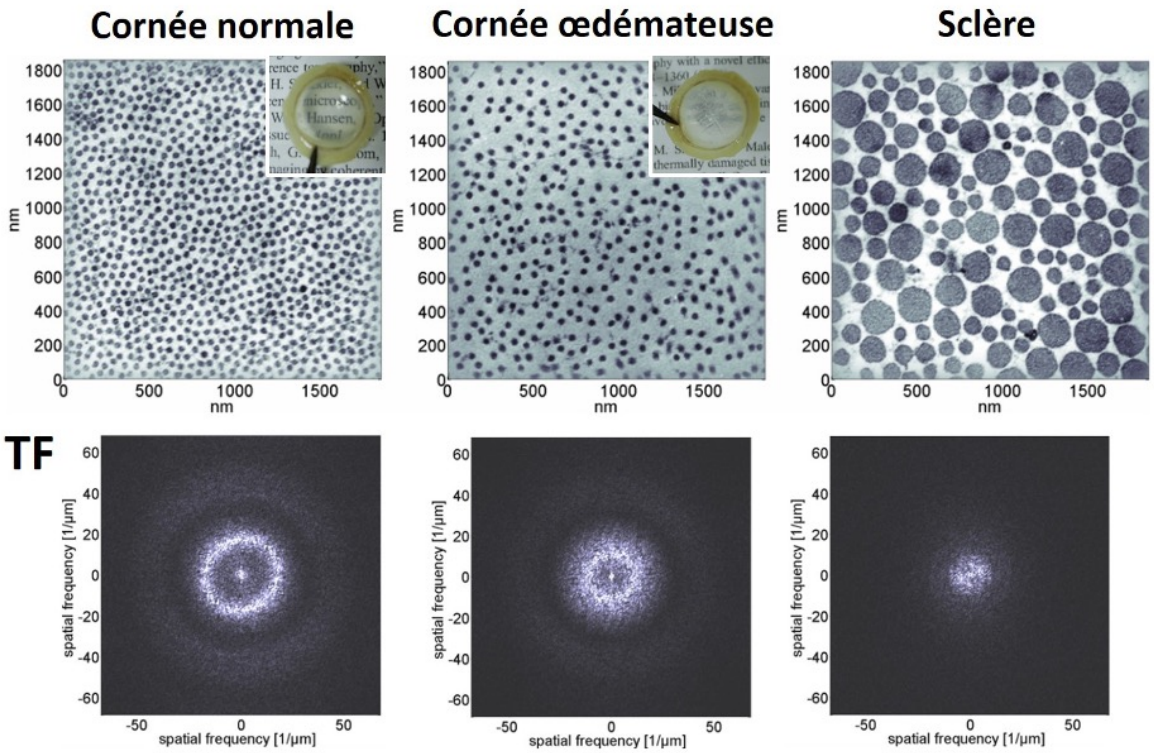

Figure 1.11: Top: Transmission electron microscopy images of a healthy cornea (a), an edematous cornea (b), and the sclera (c). Bottom: Two-dimensional Fourier transforms of the corresponding microscopy images. Taken from [2]

fibrils is disrupted, or there are structural irregularities within the cornea. In that case, the scattering can occur over wider angles, affecting corneal transparency and image formation on the retina.

To accurately model light scattering in the cornea, it is necessary to consider its various components. Light scattering within the stroma occurs primarily due to two types of scatterers: collagen fibrils at the nanometer scale and keratocytes at the micrometre scale. The model presented in this section is based on the methodology developed by a previous PhD student in the team, Romain Bocheaux [2].

Hypothesis

The stroma consists of lamellae containing collagen fibrils oriented in a predominant direction, which varies between lamellae. The other components considered in the model are keratocytes and lacunae. Keratocytes are the cells that synthesize collagen, while lacunae are structures formed by two disconnected lamellae in the case of oedema, creating an elongated region without collagen fibrils.

Highly diffusing corneas can be diagnosed using a biomicroscope, or by visual inspection, so they do not need precise diffusion analysis. The established model is then limited to weakly diffusing corneas that require precise methods to detect subtle changes

in diffusion. From a physical perspective, this represents corneas with a mean free path of diffusion (l_s) on the order of the corneal thickness ($Z_{tissue} \approx l_s$).

Radiative transfer equation

Radiative transfer (also called radiation transport) is the physical phenomenon of energy transfer in the form of electromagnetic radiation. The propagation of radiation through a medium is affected by absorption, emission, and scattering processes. The radiative transfer equation describes the evolution of radiance during propagation. It differs from the luminance defined in photometry, which considers the retinal response a function of wavelength. Since we are not concerned with the retinal response here, we will use the term luminance to refer to radiance, denoted as L.

The radiative transfer equation is a partial differential equation involving terms for loss through diffusion or absorption and for gain through diffusion in the considered direction or from a source. In our case, we only consider losses through diffusion (since the cornea is a tissue with low absorption in the visible spectrum), and we consider a gain term corresponding to the scattered radiance in the considered direction. The radiative transfer equation can thus be written as follows:

$$\vec{u} \cdot \vec{\nabla} L(\vec{r}, \vec{u}) = \underbrace{-\frac{1}{\ell_s} L(\vec{r}, \vec{u})}_{loss} + \underbrace{\frac{1}{4\pi \ell_s} \int_{4\pi} p\left(\vec{u}, \vec{u}'\right) L\left(\vec{r}, \vec{u}'\right) \mathrm{d}\Omega'}_{gain} \tag{1.1}$$

where p($\vec{u}$, $\vec{u'}$) is the phase function. L($\vec{r}$) is the radiance, representing the energy flux at a point $\vec{r}$ in the direction $\vec{u}$ [$W \cdot m^{-2} \cdot sr^{-1}$].

The left-hand side of the radiative transfer equation describes the spatial evolution of radiance. The right-hand side consists of a negative term representing the loss of radiance in the direction $\vec{u}$ during propagation through the medium, resulting in exponential decay with attenuation described by the mean free path of diffusion. The second term represents scattering events contributing to the radiance increase in the direction $\vec{u}$.

The phase function p($\vec{u}$, $\vec{u'}$) represents the probability of a change in the propagation direction of the wave from direction $\vec{u'}$ to direction $\vec{u}$. This function describes the scattering process by different types of scatterers. The colatitude angle between $\vec{u}'$ and $\vec{u}$ is denoted θ. By projection on the axis of propagation z, we define $\mu = \cos\theta$ and $p^0(\mu, \mu') = \frac{1}{2\pi} \int_0^{2\pi} p(\mu, \mu', \phi - \phi') \, \mathrm{d}\phi'$.

The luminance is divided into two terms, one corresponding to the ballistic intensity I_{bal} and the other to the intensity scattered in all directions except towards the front L_{diff}:

$$L(z, \theta) = I_{\mathrm{bal}}(z) \delta(\cos\theta - 1) + L_{\mathrm{diff}}(z, \theta) \tag{1.2}$$

By inserting the expression of the ballistic intensity into the radiative transfer equation

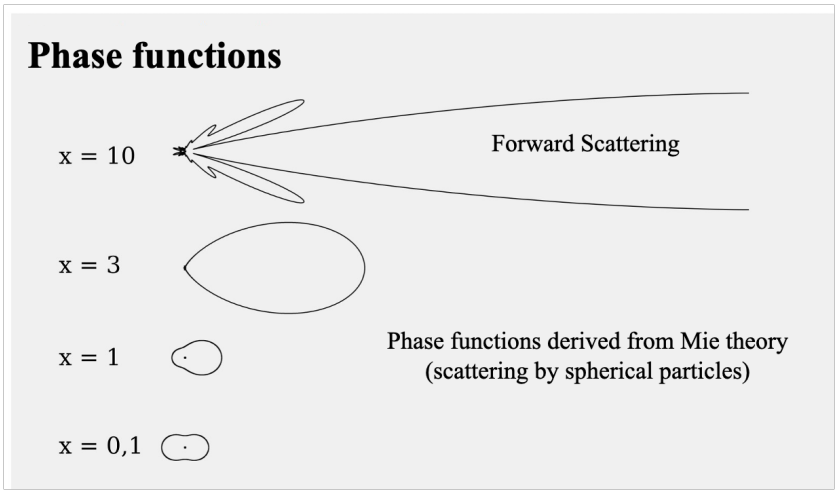

Figure 1.12: Phase functions and direction of diffusion. The direction of diffusion depends on the geometry of the considered particle and its size r relative to the wavelength λ of the incident radiation, expressed by the parameter $x = \frac{r}{lambda}$. Illustrations for a spherical particle. Taken from [23].

projected on the z axis and by integrating on $\mu = \cos\theta$, we get:

$$\int_{-1}^{+1} \mu \frac{\partial I_{bal}}{\partial z}(z)\delta(\mu-1)\mathrm{d}\mu = -\frac{1}{\ell_\mathrm{s}} I_{bal}(z) \int_{-1}^{+1} \mathrm{d}\mu + \frac{I_{bal}(z)}{2\ell_\mathrm{s}} \int_0^{\pi} p^0(\mu,1)\mathrm{d}\mu$$

$$\Leftrightarrow \frac{\partial I_{bal}}{\partial z}(z) = -\frac{1}{\ell_\mathrm{s}} I_{bal}(z) \Rightarrow I_{bal}(z) = I_0 \exp\left(-\frac{z}{\ell_\mathrm{s}}\right) \quad (1.3)$$

which is the Beer-Lambert equation with ℓ_s the mean free path of diffusion of the medium.

By doing the same for the diffused luminance, we obtain:

$$\frac{\partial L_{diff}}{\partial z}(z,\theta)\cos\theta = -\frac{1}{\ell_\mathrm{s}} L_\mathrm{diff}(z,\theta) + \frac{1}{2\ell_\mathrm{s}} p^0(\theta,0) I_0 \mathrm{e}^{-\frac{z}{\ell_\mathrm{s}}} + \frac{1}{2\ell_\mathrm{s}} \int_{-1}^{+1} p^0(\theta,\theta')\, L_{riff}(z,\theta')\, \mathrm{d}\cos\theta' \quad (1.4)$$

where multiple scattering is neglected (weak scattering approximation). The solution for the diffused luminance, with a boundary condition of absence of diffusion coming from the endothelium $(z = Z)$, is written:

$$L_\mathrm{diff}(z,\theta) = \frac{p^0(\theta,0)}{2(0-\cos\theta)} I_0 \left[\exp\left(-\frac{z}{\ell_\mathrm{s}}\right) - \exp\left(-\frac{(\cos\theta-0)Z+z}{\ell_\mathrm{s}\cos\theta}\right)\right] \quad (1.5)$$

Average mean free path of scattering

The exponential decrease in ballistic intensity depends solely on the mean free path of diffusion $\ell_\mathrm{s}$du corneal stroma. This is written:

$$\frac{1}{\ell_\mathrm{s}} = \frac{1}{\ell_\mathrm{K}} + \frac{1}{\ell_\mathrm{c}} \quad (1.6)$$

with ℓ_{K} the mean free path of diffusion associated with keratocytes and lakes and ℓ_{c} that is associated with collagen fibrils.

Keratocytes and lakes are laterally several microns wide structures and can therefore be considered Mie-type scatterers for wavelengths in the visible spectrum. Thus their scattering cross section σ_K is weakly dependent on the wavelength, and their size influences the angular distribution of the scattered intensity.

The mean free path of diffusion associated with keratocytes and lakes ℓ_{K} is written:

$$\ell_K = \frac{1}{\rho_K \sigma_K} = \frac{1}{2\pi\rho_K R^2(1-\cos\delta)} \tag{1.7}$$

with ρ_K their density and $\delta = 4\pi e(m-1)/\lambda$ the phase difference of light at wavelength λ after passing through a keratocyte modelled as a flat cylinder of diameter $2R$ and thickness e having an optical index ratio $m = n_{\mathsf{K}}/n_e$ with the extra-cellular medium.

Collagen fibrils can be modelled as dielectric needles of infinite length (two-dimensional geometry) [13]. The diffusion cross-section of a collagen lamella σ_{c} is calculated from the diffusion cross-section of a single fibril σ_f [19] and the pair correlation function $g(\vec{r})$. The pair correlation function translates the local order of the fibrils by describing the variation of the density of particles (here the collagen fibrils) as a function of the radial distance to a reference particle; it can be measured from transmission electron microscopy images of the corneal stroma (acquired orthogonally to the direction of the lamella) using the two-dimensional Percus-Yevick equation [16][10][2].

The mean free path of diffusion associated with the collagen lamellae ℓ_{c} is written:

$$\ell_c = \frac{1}{\rho_c \sigma_{\mathsf{c}}} = \frac{1}{\rho_c \sigma_f \left[1 + 2\pi\rho_{\mathsf{c}} \int_0^\infty r[g(r)-1]J_0^2\left(k_0 r\right)\mathsf{d}r\right]} \tag{1.8}$$

σ_f with the diffusion cross-section of a single fibril $[\mathsf{m}]$, ρ_{c} the surface density of the collagen fibrils which can be considered homogeneous in the corneal stroma $\left[\mathsf{m}^{-2}\right]$, $g(r)$ the correlation function of fibril pairs in the corneal stroma as a function of r the radial distance to a reference fibril, J_0 the Bessel function of the first kind and $k_0 = \frac{2\pi}{\lambda}$ the wave number of the radiation considered.

The orders of magnitude of the mean free path of scattering associated with the different types of scatterers were estimated from data from the literature (for the optical indices and the density of the scatterers) and transmission electron microscopy images (for the function correlation of fibril pairs). The effective mean free path of the stroma of a normal cornea has been calculated: it is of the order of 3.6 mm at 550 nm (the peak of sensitivity of the human eye) and 18 mm at 840 nm (the wavelength of the clinical devices at the Quinze-Vingts hospital).

1.3.3 PSF

The point spread function (PSF) describes how an imaging system responds to a point source of light or a point object. In simpler terms, the PSF illustrates how light from a single point in an object is spread out or blurred in the final image due to various factors within the imaging system. The PSF is typically represented as a two-dimensional function or image. Ideally, PSF would be a perfect point in an imaging system, but it is usually a bell-shaped or Gaussian-like curve in real-world systems.

Understanding the PSF is crucial in medical imaging. The PSF represents the cumulative effect of all the phenomena light encounters along its path, containing factors such as aberrations and scattering.

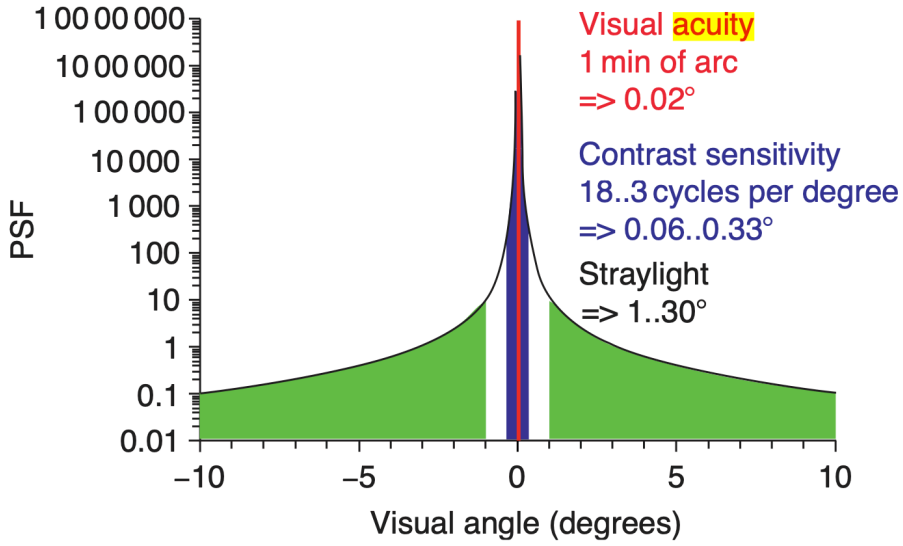

Figure 1.13: Angular Point Spread Function on the retina. The red portion defines visual acuity, the blue portion represents contrast sensitivity, and the green portion corresponds to glare. The PSF is measured in steradians per square degree, and the integral over solid angle is normalized. Taken from [22]

Figure 1.13 displays the Point Spread Function from a clinical perspective. [22] Within the PSF, distinct regions hold critical significance:

- **Central Region:** The PSF's central portion defines visual acuity.
- **Larger Angles:** Beyond the central region, slightly larger angles within the PSF define contrast sensitivity (0.06º-0.33º), a measure of how well the eye can discriminate the various shades of gray. Larger angles correspond to the phenomenon of glare. Glare corresponds to instances where excessive scattered light interferes with the clarity of the image (1.3º).

An increased scattering within the optical system leads to the broadening of the PSF, decreasing visual acuity, and increasing glare levels, further impairing the overall image quality. Therefore, fully comprehending the PSF is vital in optimising medical imaging processes and ensuring the delivery of high-quality diagnostic information.

Visual Acuity

Visual acuity (VA) is a measure of the ability of the eye to distinguish shapes and the details of objects at a given distance. It can be expressed as a fraction, where the numerator represents the testing distance and the denominator indicates the distance a person with normal vision can read the same line. For example, if someone can read the 6/6 line on the chart, they can read at 6 meters what a person with normal vision can read at 6 meters. Visual acuity measurements assess the impact of refractive errors (e.g., myopia, hyperopia, astigmatism), cataracts, and other eye conditions on an individual's ability to see clearly, a necessary metric for determining corrective measures. However, visual acuity measurements only capture some aspects of visual function. Factors such as contrast sensitivity, colour vision, peripheral vision, and visual processing abilities also play a role in overall visual perception and may not be fully assessed through visual acuity testing alone.

In a PSF of the eye, the visual acuity is defined as the area of the small-angle regime (-0.02º-0.02º) [22]. A person of regular sight, measured as 6/6, can differentiate two objects with a visual angle of 30 seconds (0.008º) to 1 minute (0.017º) of arc [12].

In summary, visual acuity is a foundational metric to assess the quality of the vision and a primary tool for diagnosis and treatment selection. However, it must consider other complimentary metrics to assess thoroughly the PSF of the corresponding eye and the conditions at larger angles (>0.02º)

Strehl Ratio

The Strehl ratio is a measure of the quality of optical image formation. It indicates how well the system focuses light compared to an ideal, diffraction-limited optical system. The Strehl ratio is between 0 and 1, with a hypothetical, perfectly aberration-free optical system having a Strehl ratio of 1 and lower values indicating a degradation in image quality.

To calculate the Strehl ratio, one must know the optical system's actual point spread function (PSF) and compare it to the ideal PSF limited solely by diffraction (i.e., the theoretical maximum). The formula for calculating the Strehl ratio is:

$$S = \frac{I_{actual,max}}{I_{ideal,max}} \tag{1.9}$$

where:

- $I_{actual,max}$ is the maximum intensity of the actual PSF,
- $I_{ideal,max}$ is the maximum intensity of the ideal PSF.

In the case of normalized intensities, the Strehl Ratio will be the maximum intensity of the actual PSF.

Its single-value nature provides simplicity when evaluating the performance of an optical lens and facilitates comparing different optical systems or conditions. This parameter is, however, limited due to its lack of aberration specificity and high sensitivity to medium-high aberrated optical systems. It does not provide information about the specific types or nature of aberrations present in an optical system. Heavily aberrated corneas can have complex and diverse aberration profiles, including coma, trefoil, and spherical aberrations, which can affect vision differently. Its value decreases significantly with even moderate aberrations. In heavily aberrated corneas, such as those with advanced keratoconus or significant irregular astigmatism, the Strehl Ratio may be very low, making it challenging to discern meaningful differences in optical quality.

In conclusion, characterizing the point spread function of the cornea through the Strehl Ratio has meaning and importance in an initial analysis in which one wants to have a single value to characterize the state of the cornea generically.

1.4 Clinical techniques for measuring corneal transparency

The clinical diagnostic of diseased corneas is done mainly through contact-free devices such as slit lamps and Optical Coherent Tomography. However, contact devices are also used, like confocal microscopy devices.

A **slit lamp** is a stereoscopic biomicroscope with a high-intensity illumination source that projects a thin sheet of light into the eye from a halogen source at an adjustable length, width and incidence angle. At the same time, a microscope objective allows for examining the scattered light at various magnifications. The lamp facilitates an examination of the human eye's anterior and posterior segments, including the eyelid, sclera, conjunctiva, iris, natural crystalline lens, and cornea. A second hand-held lens is used to examine the retina.

In some cases, the observer supplements this observation by subjectively comparing it using an arbitrary grading scale (0 to 4 or 5, with 0 indicating a transparent cornea and 4 or 5 indicating an opaque cornea). The figure 1.14 displays examples of such images, showcasing extreme cases where the difference is apparent. Due to this method's subjective and qualitative nature, its outcomes are observer-dependent, difficult to standardize, and lack reproducibility. Consequently, several research teams have proposed alternative approaches to quantify and evaluate corneal transparency objectively. The first alternative is to enhance the slit lamp biomicroscope by incorporating polarizers to differentiate between specular reflection and scattered light. However, the axial resolution remains limited, and the analysis could be more precise. The other method is using Scheimpflug photography images. This method allows for obtaining cross-sectional images of the entire focused cornea by tilting the sensor relative to the objective. From Scheimpflug photography images, the authors calculate intensity averages of the hyper-

Figure 1.14: Top: Image of a slit lamp biomicroscope. Bottom: Slit lamp images of a healthy cornea with low scattering (on the left) and a pathologic cornea with high scattering (on the right). Taken from [2]

reflective area observed in these images. Nevertheless, it is crucial to highlight that researchers have only validated the repeatability of this method in laboratory settings.

Confocal microscopy is an advanced imaging technique based on the Marvin Minsky principle that provides high-resolution, three-dimensional images of specimens using a laser scanning system and a confocal pinhole to eliminate out-of-focus light. It is widely used to visualize the evolution of disorders in the bowman and stroma layers. In this

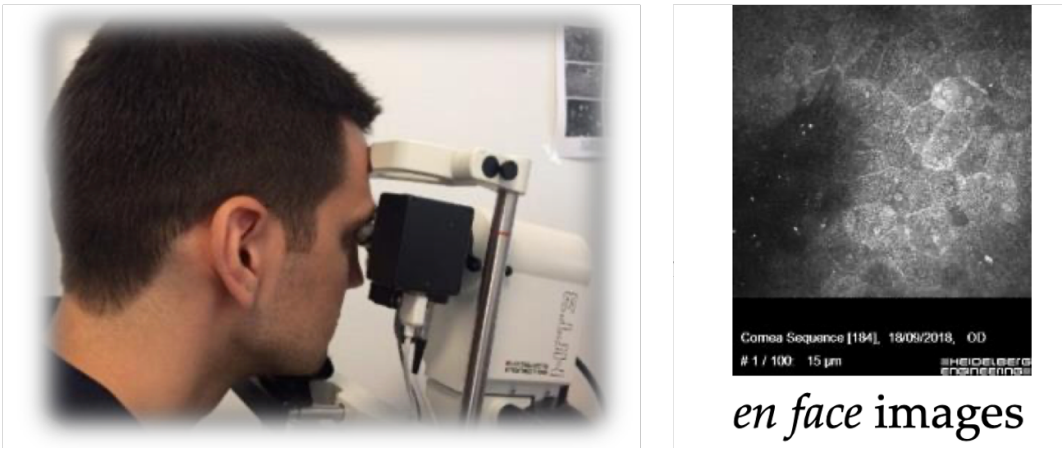

Figure 1.15: Confocal Microscopy device and typical image obtained. Taken from [2]

technique, the laser beam focuses on a specified specimen point at a specified depth, and a detector captures the emitted light. The crucial part of this method is a pinhole aperture in front of the detector that cuts off signals out of focus, allowing only the signals from the illuminated spot to enter the light detector.

To solve the problem of a limited field of view caused by single-point illumination, the instrument utilizes thousands of tiny spots of light to scan a small region of tissue. These spots are then reconstructed to create a usable field of view. Even though this is the technique with the higher resolution among the three presented, the inconvenience of confocal microscopy is the need for physical contact between the microscope objective and the cornea, which is uncomfortable for the patient and, therefore, not used as a routine examination.

The last typical ocular exam performed is **Optical coherence tomography (OCT)**. This non-invasive imaging technique uses low-coherence light to capture two and three-dimensional images from the optical scattering media (eye tissue). It can be used to study

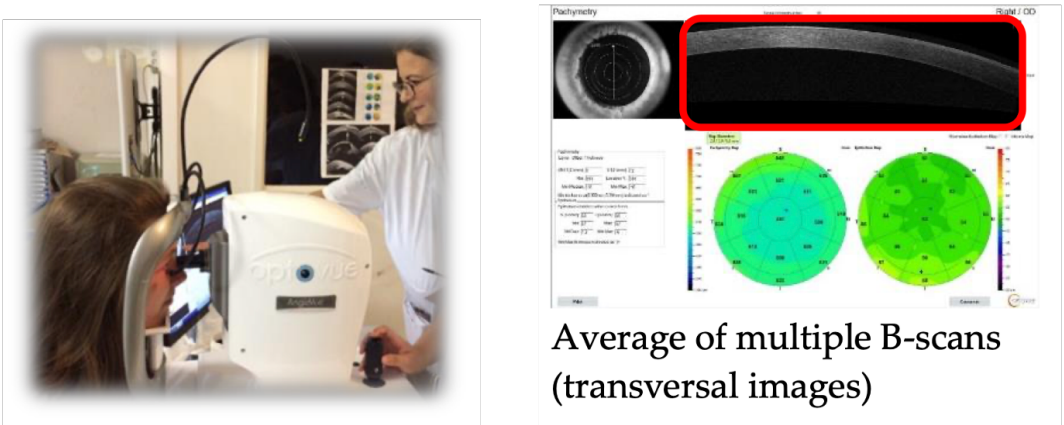

Figure 1.16: Clinical OCT device and analysis. Taken from [2]

anomalies in the cornea and the retina. For the latter, it is common to use a dilating eye drop to widen the pupil to make it easier to examine the retina.

This technique will be studied in more depth in the next section 1.5 since it is the laboratory method to study the cornea's transparency.

1.5 Principles of OCT

Since clinical measurements can only be performed in backscattering, the imaging techniques that will interest us are those based on phenomenon. The technique used for this thesis project is the OCT, one of the most commonly used depth-resolved imaging methods in ophthalmology. During the past two decades, optical coherence tomography (OCT) has become one of the most commonly used depth-resolved imaging methods in ophthalmology. OCT technology has revolutionized patient care by enabling high-resolution, non-invasive, in vivo imaging of ocular tissues.

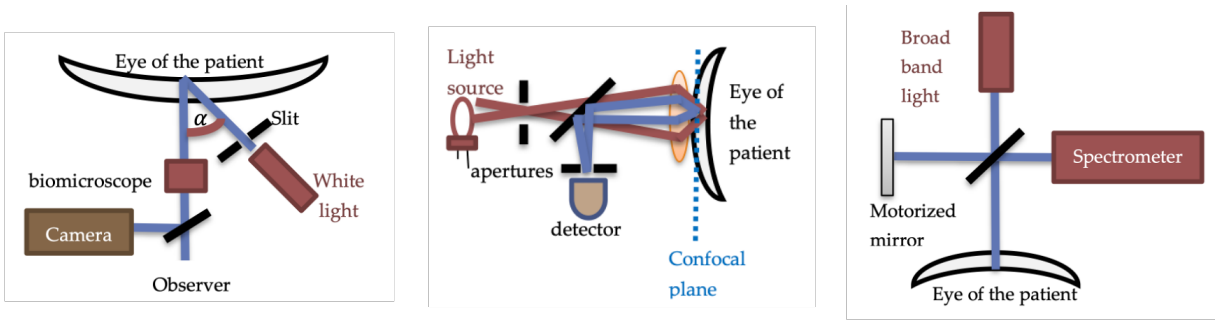

Axial Resolution: ~ 30 μm | Axial Resolution: ~ 7.6 μm | Axial Resolution: ~ 10 μm

a) b) c)

Figure 1.17: Diagrams: a) Slit Lamp b) Confocal Microscopy c) OCT. Taken from [2]

OCT is an optical imaging method that utilizes the time-of-flight measurement of reflected waves from scattering tissues. While the basic concept is similar to ultrasound imaging, it relies on the interference of light waves rather than sound waves.

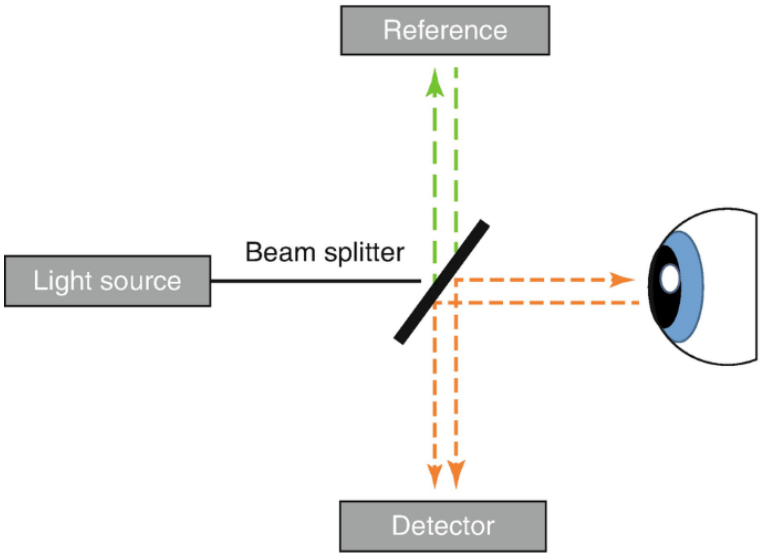

Figure 1.18: Basic principle of OCT. Taken from [21]

To obtain accurate depth information, OCT employs an interferometer to measure the path length difference between a reference beam and a sample beam. By understanding the principles underlying different techniques, we can gain insights into their unique advantages, limitations, and applications in biomedical imaging.

1.5.1 Time-domain OCT (TD-OCT)

Time-Domain Optical Coherence Tomography (TD OCT) achieves micrometre axial resolution using a low-coherence light source. This light source enables the interference signal to be recorded only when the optical path length of the sample and reference arm

matches the narrow coherence length. The reference arm is then scanned to align the optical path length with the reflections within the sample. A reflectivity depth profile or A-scan is generated by demodulating the recorded interference signal at different depths or relative time delays.

In TD OCT, the imaging process involves scanning the length of the reference arm, allowing the selection of different cross-sectional planes along the z-axis. Additional scanning along the x or y-axis is achieved using oscillating mirrors. This setup is illustrated in Figure 1.19. One of the notable advantages of OCT is its independence of axial and lateral resolutions, which differs from conventional microscopy systems, where these resolutions depend on the optical system used.

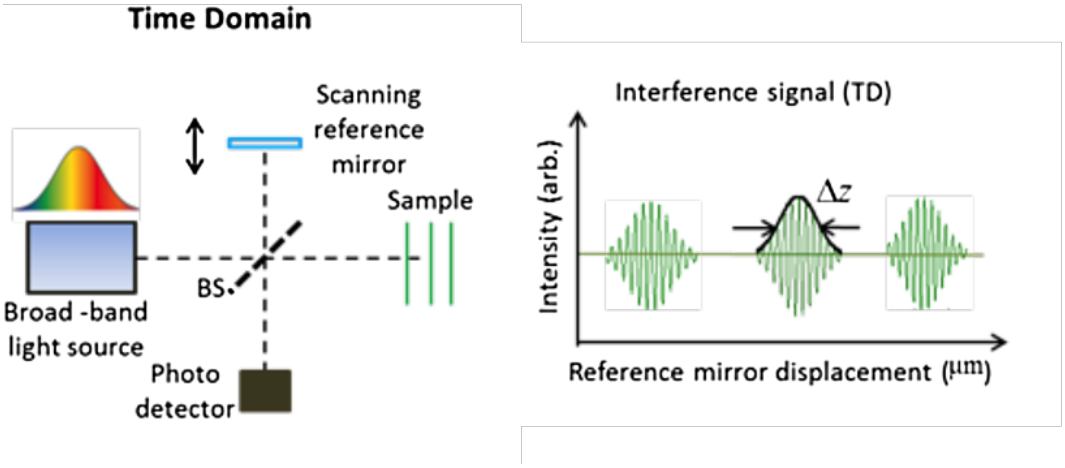

Figure 1.19: Basic principle of TD-OCT. Taken from [6]

The lateral resolution in OCT is determined by the beam's focusing (i.e., the numerical aperture NA) and is limited by diffraction. For a Gaussian beam with a central wavelength λ, the lateral resolution, defined by the full width at half-maximum of the beam, can be expressed as:

$$\delta x = 0.37 \times \frac{\lambda}{NA} \tag{1.10}$$

Conversely, the axial resolution in OCT does not rely on the optical system but instead on the spectral properties of the light source. The axial resolution is equal to the coherence length of the source, given by:

$$\delta z = 2\ln(2) \times \frac{\lambda^2}{\Delta\lambda^2} \tag{1.11}$$

where λ is the central wavelength, $\Delta\lambda$ is the spectral bandwidth, and n is the refractive index.

Thus, TD OCT offers high axial resolution due to its low-coherence light sources and enables precise imaging of biological tissues and other samples with micrometre-level

detail.

1.5.2 Spectral-domain OCT (SD-OCT)

Spectral Domain Optical Coherence Tomography (SD-OCT) is an advanced image technique that succeeded TD-OCT. This technique uses innovative principles based on Fourier domain analysis to overcome the limitations associated with slow acquisition speed and susceptibility to motion artefacts of TD-OCT. SD-OCT relies on lateral scanning alone, greatly accelerating the acquisition times (up to a factor of 50-100) [27]. With improved signal-to-noise ratios [3], SD-OCT propelled the gold standard for ophthalmic imaging systems, widely adopted in clinical practice [26].

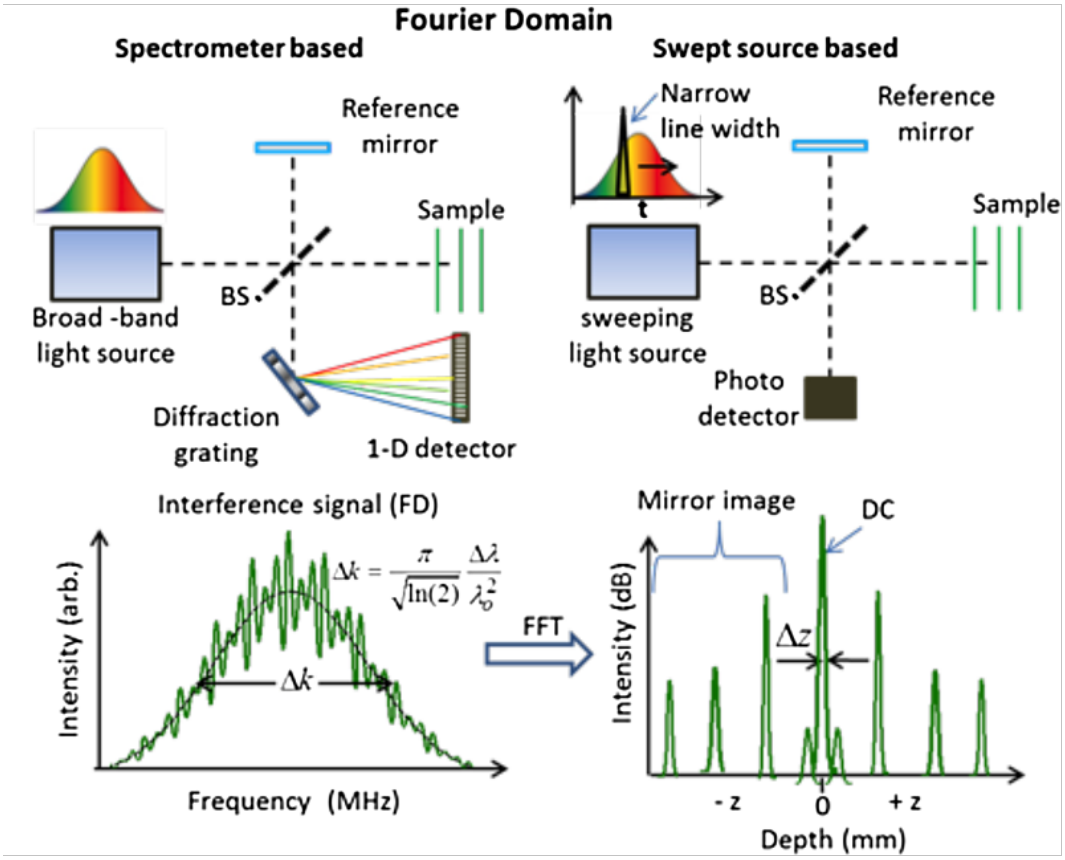

Figure 1.20: Basic principle of SD-OCT. Taken from [6]

SD-OCT's fundamental principle and foremost difference is its spectral encoding of depth information. Instead of moving a reference mirror, the collected interferential signal's frequency (or wavelength) encodes depth. This method enables instantaneous acquisition of A-scans, improving imaging speed and reducing the impact of motion artefacts. The transformation of the frequency-encoded data through Fourier analysis translates the information from frequency to axial reflectivity profiles of the sample enabling visualization of structural details within biological tissues with enhanced depth and resolution.

There are two main implementations of this type of OCT:

- replacing the detector with a spectrometer or introducing a dispersive element (e.g., grating or prism) before a linear detector, resulting in Spectral Domain OCT (SD-OCT) (left side of figure 1.20);
- utilizing a light source capable of sequentially emitting narrow spectral bands from a broader spectrum, resulting in Swept Source OCT (SS-OCT) (right side of figure 1.20).

Concluding, SD-OCT has revolutionized non-invasive imaging by providing fast, high-resolution scans of biological tissues leading to its widespread adoption in ophthalmic diagnostics, improving patient care and clinical outcomes.

1.5.3 Full-field OCT (FF-OCT)

Full-Field Optical Coherence Tomography (FF-OCT) is another imaging technique with advantages in visualizing biological tissues and structures at high resolutions. Unlike TD-OCT methods that do B-scans, FF-OCT captures en-face images in a wide-field configuration at a specific depth within the tissue, allowing rapid, label-free and non-destructive imaging of samples.

The fundamental concept of FF-OCT involves utilizing a Michelson interferometer with a Linnik configuration (Fig.1.21). In this setup, employing a spatially incoherent light source with a variation of the path length difference generates the interference images. These interference images, acquired by a CCD or CMOS camera, are combined using phase shift interferometry methods. The Linnik configuration incorporates high numerical aperture microscope objectives in both the sample and reference arms, enabling the capture of high-resolution images orthogonal to the illumination beam. This setup also ensures flexibility in adjusting the optical path lengths and focus, allowing for diverse imaging scenarios.

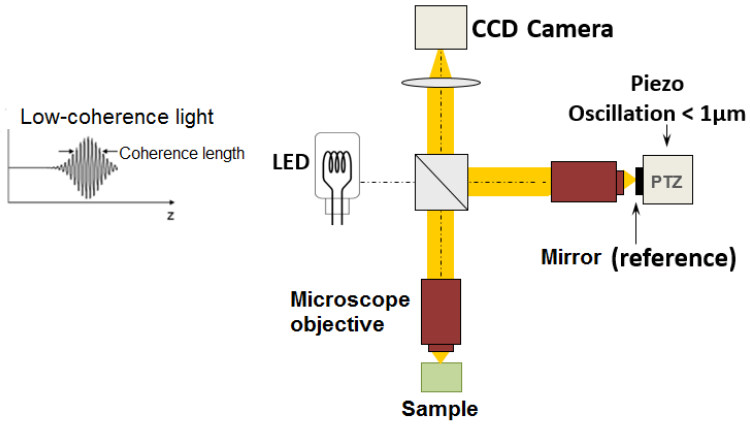

Figure 1.21: Basic principle of FF-OCT. Taken from [24]

The axial resolution of FF-OCT mainly depends on the coherence length of the light source, whose theoretical value is calculated using Eq.(1.12):

$$\delta z = \frac{l_c}{2} \approx \frac{2\ln 2 \cdot n\pi \cdot \lambda_0}{\Delta\lambda}, \tag{1.12}$$

where l_c is the coherence length, $\Delta\lambda$ and λ_0 are the spectral bandwidth and central wavelength of the light source, respectively, and n is the refractive index of the medium, which equals 1 in air and is between 1.3 and 1.5 in biological tissue. Equation 1.12 can be a criterion for selecting a light source.

The transverse resolution of FF-OCT is determined by the half peak width of the transverse point spread function, whose theoretical value is calculated using Eq. (1.13):

$$\delta x \approx \frac{\lambda_0}{2 \cdot NA}, \tag{1.13}$$

Here, NA is the numerical aperture of the microscope objective, and λ_0 is the central wavelength of the light source.

Overall, FF-OCT is a powerful and versatile tool offering real-time, non-invasive, high-resolution visualization of biological samples.

Chapter 2

Data Acquisition and Image Analysis

After establishing the principles of the human eye, the cornea diffusion model and the OCT principles, evaluating the transparency conditions and physical properties of a set of corneas is interesting to start building a robust cornea characterisation model. To achieve this, it is necessary first to segment the keratocytes. This chapter will explore different segmentation methods and extensively analyse both methods to choose the most adequate one for the case study.

2.1 Cornea Imaging

2.1.1 Acquisition of cornea images

The cornea images utilized in this study were acquired through a state-of-the-art OCT machine within our laboratory. The machine employed for this purpose is produced by DAMAE Medical. It offers exceptional imaging capabilities due to its high axial and transverse resolution of 2,6 μm and 0,99 μm, respectively. The acquisition process involved corneas in a fixed and non-fixed state. The former pertains to corneas under stable conditions, preserving their essential properties such as depth and collagen organization. The latter pertains to corneas that have undergone deswelling, resulting in dehydration. This process induces alterations in corneal depth, thereby affecting the arrangement of structures and cells within the cornea.

The grayscale images obtained are of the z-stack type, a succession of 2D planes at progressive depths forming a 3D representation of a section of the cornea of size 1200 μm x 500 μm, as shown in figure 1.6.

A diverse set of cornea images was at our disposal during this thesis. One group consisted of fixed cornea images acquired in a previous experiment. The remaining

images, which were non-fixed, were obtained throughout the thesis's duration, approximately halfway through the research. These two distinct groups of cornea images, acquired through different cornea experimentation sessions, are detailed in Table 2.1. As discussed in the following sections, these corneas were used to study the efficiency of two keratocyte segmentation methods (already referred to in table 2.1).

Table 2.1: Datasets Available for study

Cornea	Use	Acquisition Time Point
Fixed	Conventional Segmentation 3DUNET training	-
Non-Fixed 1A	3DUNET training	-
Non-Fixed 1B		4h after 1A
Non-Fixed 1C		3h after 1B
Non-Fixed 2A	3DUNET test	-
Non-Fixed 2B		2h after 2A
Non-Fixed 3A		-
Non-Fixed 3B		6h after 3A
Non-Fixed 3C		3h after 3B

2.1.2 Contrast Levels

This section aims to elucidate the significance of the contrast levels in OCT images. Higher contrast values typically signify a clearer demarcation between layers or features, making it easier to identify and segment various components of the cornea.

Figure 2.1 shows the visual contrast differences between the fixed and non-fixed corneas images available. As one can see, the fixed cornea has higher and uniformly distributed visual contrast, resulting in well-defined keratocytes. In disparity, the non-fixed cornea presents low contrast values in the extremes of the image. To quantify these differences, the RMS contrast (equation 2.1) was calculated for the 3D image considering three different Regions Of Interest (ROI) of the same size, divided by the x-axis of the image.

$$Contrast_{RMS} = \sqrt{\frac{1}{MN}\sum_{i=0}^{N-1}\sum_{j=0}^{M-1}(I_{ij} - \bar{I})^2} \tag{2.1}$$

Where:

- I_{ij}: Intensities at the (i, j)-th element of the two-dimensional image of size $M \times N$.
- $\bar{I}$: Average intensity of all pixel values in the image.
- I: Image with pixel intensities normalized in the range $[0, 1]$.

The choice of the RMS contrast is supported by its standard use in the medical field and statistical robustness. It is less sensitive to outliers or noise in the image, making it suitable for images with some noise.

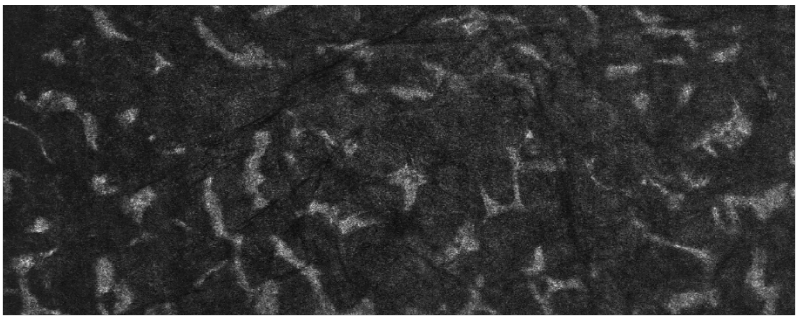

(a) Fixed cornea

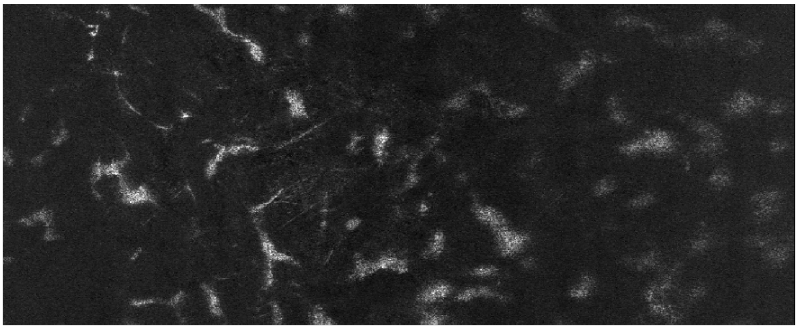

(b) Non-fixed cornea

Figure 2.1: Contrast differences between fixed and non-fixed cornea images

Figures 2.3 and 2.2 show the contrast variation for fixed and non-fixed corneas, while Table 2.2 resumes the measured mean contrast. The differences between the fixed image are evident compared to its counterparts. The former presents similar levels of contrast throughout the entire depth, and the histograms of the ROIs are close to each other with slight differences. In comparison, the latter has a high contrast in the centre region, allowing well-defined objects. However, the two lateral ROIs have significantly lower contrast, increasing the complexity of the analysis since the object's boundaries become dubious.

It is expected to have differences on non-fixed corneas due to its deswelling process that alters the structure of the stroma; however, the discrepancies along the x-axis are not expected and require further studies in the experimental procedure of OCT to check if the results are credible and due to the deswelling process or due to potential experimental oversights.

Table 2.2: Contrast statistics for three different regions of the available images

	Left ROI		**Center ROI**		**Right ROI**	
	Mean	Std Dev	Mean	Std Dev	Mean	Std Dev
Non-Fixed (mean)	19.1	1.4	26.7	3.3	18.3	3.5
Fixed	23.1	2.3	25.2	1.7	22.6	1.8

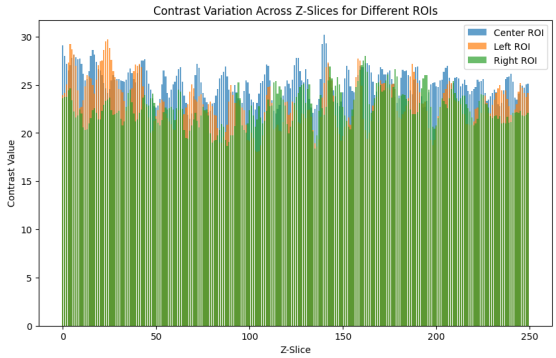

(a) Contrast variation along depth for the three different ROI

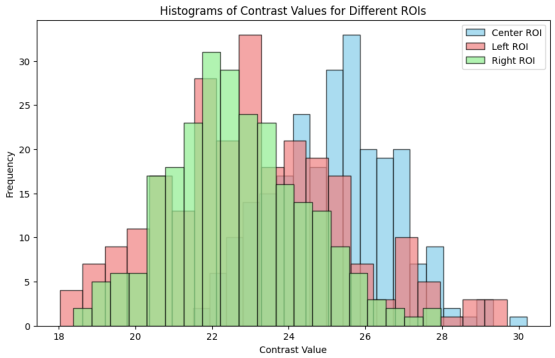

(b) Histograms of contrast values for the three different ROI

Figure 2.2: Fixed cornea

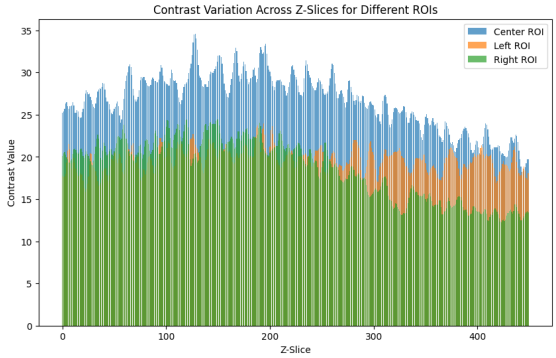

(a) Contrast variation along depth for the three different ROI

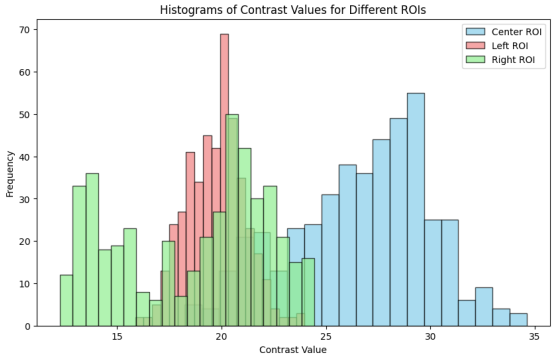

(b) Histograms of contrast values for the three different ROI

Figure 2.3: Non-Fixed cornea

2.2 Image Processing

2.2.1 Conventional Segmentation of OCT images - Workflow

Once the data acquisition phase is over, it is necessary to perform image processing in order to keep only the relevant information for our study, in this case, the keratocytes. To achieve this objective, a segmentation of the objects of interest is performed, transforming the image from grayscale to binary, where the foreground is the keratocytes and the background the regions without light reflection. The conventional segmentation process involves a set of predetermined algorithms and heuristics that operate on pixel intensities and spatial relationships within the image. This process is simple to implement, although it requires manual parameter tuning. The four main steps used are described below.

From grayscale to binary

During the initial segmentation step, the chosen method to perform binary conversion is the Otsu method. It automatically transforms the grayscale image into a binary scale by implementing a threshold that optimises the distinction between the foreground and back-

ground. This optimisation involves minimising the variance within classes while maximising the variance between classes in intensity (fig.2.4). Otsu's method can be conceptualised as a one-dimensional discrete version of Fisher's Discriminant Analysis and is equivalent to a globally optimal k-means performed on the intensity histogram.

The benefits of this method are its simplicity, computational efficiency and minimal user intervention. It also does not require prior knowledge about the processed image. However, Otsu's method assumes a bimodal intensity distribution and has the potential to not perform optimally for images with complex or non-uniform distributions.

Algorithm steps:

- **Histogram and Probability Distribution:** Compute histogram and probabilities of each intensity level

$$P(C = k) = \frac{histogram[k]}{totalpixels} \tag{2.2}$$

- **Cumulative Sum and Mean:** Calculate the cumulative sum of probabilities and the cumulative mean of intensity values.

$$P_{cum}(C = k) = \sum_{i=0}^{k} P(C = i) \tag{2.3}$$

$$\mu(C = k) = \frac{1}{P_{cum}(C = k)} \sum_{i=0}^{k} i \cdot P(C = i) \tag{2.4}$$

- **Global Mean:** Compute the global mean intensity of the image.

$$\mu_{global} = \sum_{k=0}^{L-1} k \cdot P(C = k) \tag{2.5}$$

- **Between-Class Variance Calculation:** For each possible threshold value, calculate the between-class variance as the product of the probabilities of the two classes (foreground and background) and the squared difference between their means.

$$\sigma^2_{between}(k) = P(C = k) \cdot P(\overline{C} = k) \cdot [\mu(C = k) - \mu_{global}]^2 \tag{2.6}$$

- **Threshold Selection:** Choose the threshold $k_{optimal}$ that maximises the between-class variance ($\sigma^2_{between}(k)$), resulting in the optimal separation of the two classes.

The benefits of this method are its simplicity, computational efficiency and minimal user intervention. It also does not require prior knowledge about the processed image. However, Otsu's method assumes a bimodal intensity distribution and has the potential to not perform optimally for images with complex or non-uniform distributions.

As illustrated in Figure 2.5, it becomes evident that the acquired images do not conform to the optimal conditions for applying the Otsu thresholding method. This deviation arises

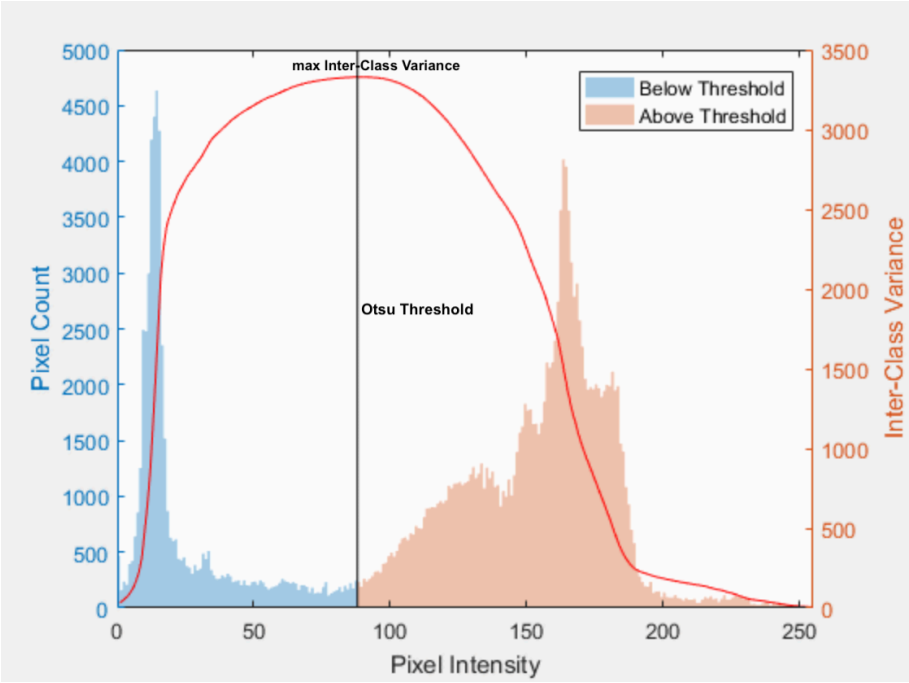

Figure 2.4: Otsu's Threshold. Example of histogram of pixel values with the corresponding Inter-Class Variance curve and the optimal threshold selection. Taken from [25]

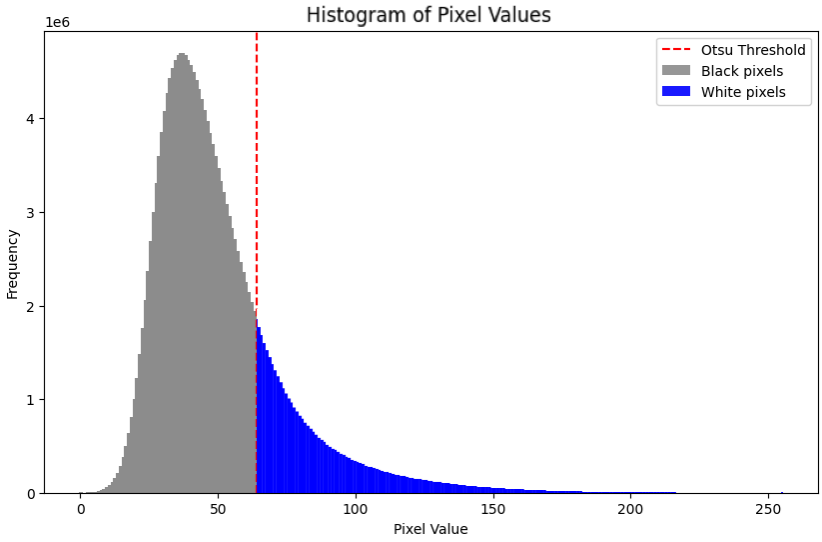

Figure 2.5: Typical pixel distribution from cornea images and corresponding Otsu Threshold for binary image conversion.

from the absence of two distinctly defined peaks, thus emphasising the preponderance of noise manifested as intermediate grayscale pixels. Despite this, the keratocytes we want to segment are in the order of hundreds of pixels in size, and the subsequent analysis of Figure 2.6 reveals that the method successfully detects nearly all objects. Consequently, this outcome adequately fulfils our requirements, enabling us to proceed with the following processing stages.

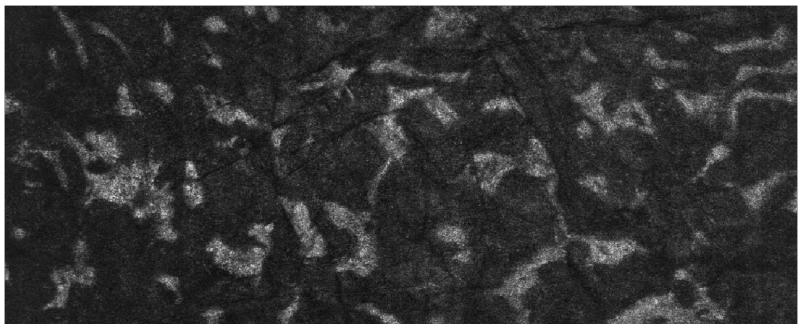

(a) 2D grayscale plane of a fixed cornea at an undetermined depth

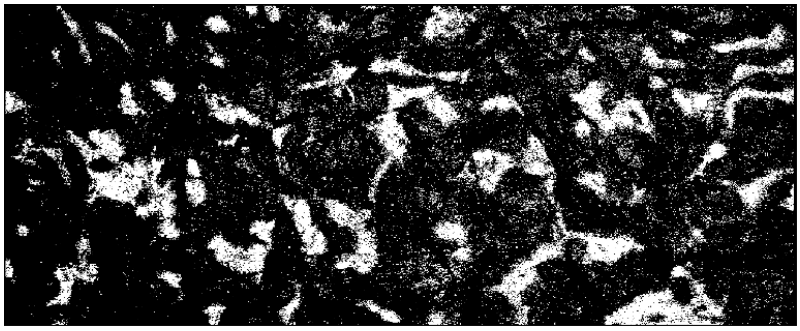

(b) Conversion to binary image through Otsu threshold

Figure 2.6: Grayscale to binary image using Otsu method

Closing: removal of small dark spots

In the second phase of conventional segmentation, applying the morphological operation known as ”closing”, defined as a dilation followed by an erosion, assumes significance by strategically refining the image. While this step could be performed before converting the grayscale image to a binary, it is optimal to perform it afterwards. Given that the images used are a collection of approximately 600 2D planes, each sized at 1200x500 pixels, employing closing after the binary transformation increases computational efficiency and reduces processing time due to the lower complexity of the information. Dilation (Figure

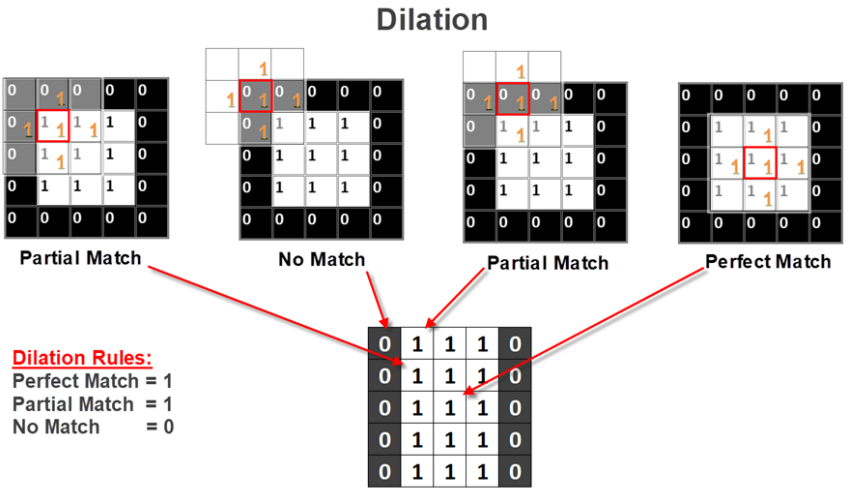

Figure 2.7: Dilation operation in a matrix. Taken from [5]

2.7) is the first phase of closing, representing a morphological operation that expands the boundaries of objects in a binary image. It involves sliding a structuring element (a small binary image) over the input image and setting the pixel in the output image to 1 if any of the ”on” pixels in the structuring element overlap with the ”on” pixels in the input image.

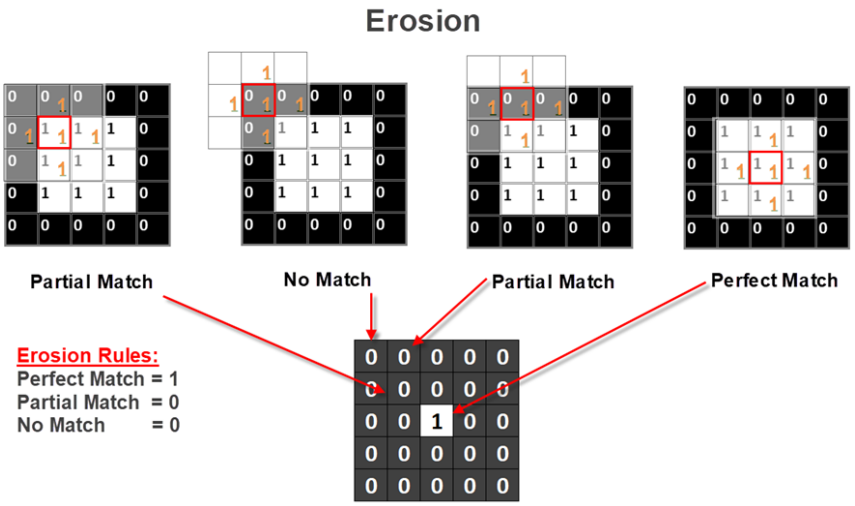

Figure 2.8: Erosion operation in a matrix. Taken from [5]

In contrast, erosion (Figure 2.9), the last step, is a morphological operation that contracts the boundaries of objects in a binary image. Similar to dilation, it involves sliding a structuring element over the input image, but the output pixel is set to 1 only if all corresponding structuring element pixels are 1 in the input image.

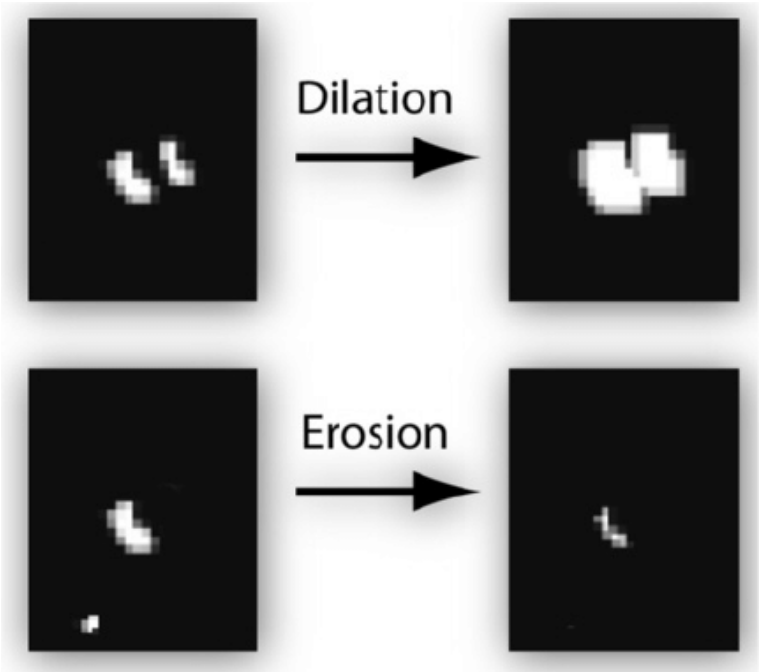

Figure 2.9: Visual effect of dilation and erosion in an image. Taken from [18]

Closing combines these two operations to effectively eliminate small, isolated noise

components (often called ”salt and pepper” noise), encompassing them during dilation and later removing them during erosion. In addition, it also fills small gaps in white regions, making them more uniform and precise.

Two of the dangers of this method are the possibility of excessive smoothing and unintentional shape-shifting if the structuring element used for dilation and erosion is too large, causing the loss of fine details of the object. To avoid these dangers and consider the rounded borders of keratocytes, we used a disk as the structural element with a few pixels radius below 10 pixels. Fig.2.11 shows the differences in the cornea images before and after the closing operation.

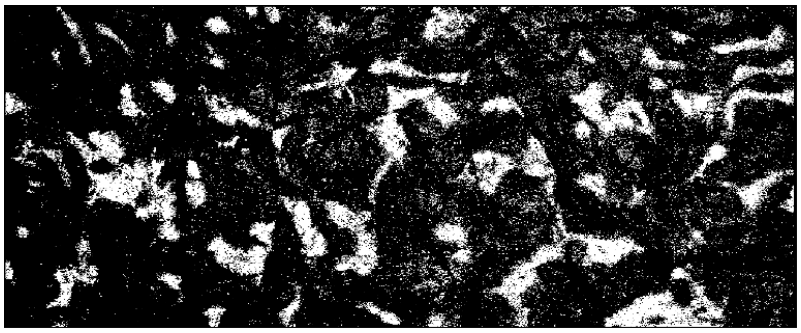

(a) Binary image

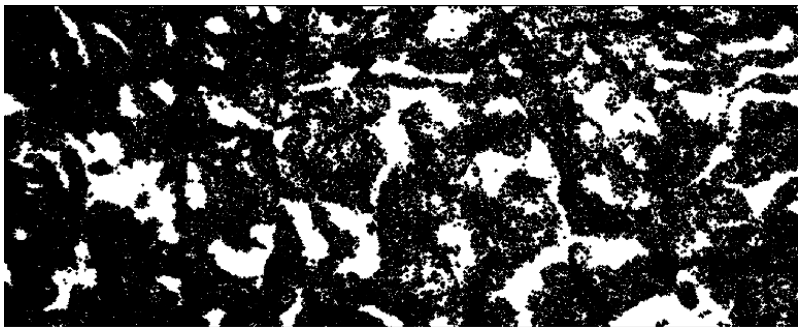

(b) Conversion to binary image through Otsu threshold

Figure 2.10: Image after Closing operation

In conclusion, this procedure acts as a noise remover and segmentation enhancement process to facilitate the path for more meaningful and appropriate analyses.

Opening: removal of small bright spots

In the third phase of conventional segmentation, applying the morphological operation known as ”opening”, defined as an erosion followed by a dilation, assumes a complementary/ reverse role to the closing operation. The binary opening is effective at noise reduction and boundary smoothing, similar to its reverse operation. However, the key advantages are its ability to break narrow connections between objects, helping to separate adjacent structures that may have been merged due to noise or other factors, and it selectively removes small-scale details while preserving the larger structures. The dangers of this operation are the potential loss of small features by eliminating small but signifi-

cant features and the potential to over-smooth and blur the edges, which could result in structural changes to the object.

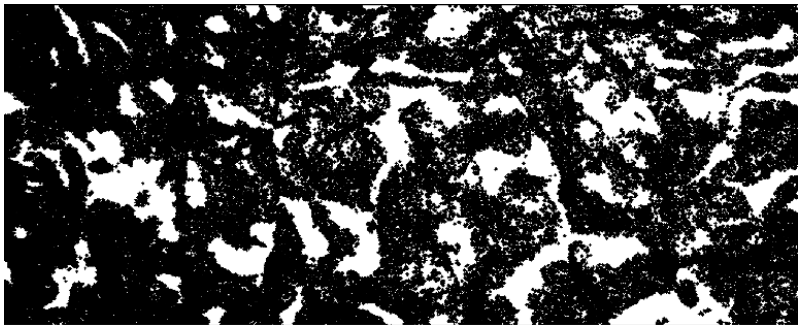

(a) Image before Opening operation

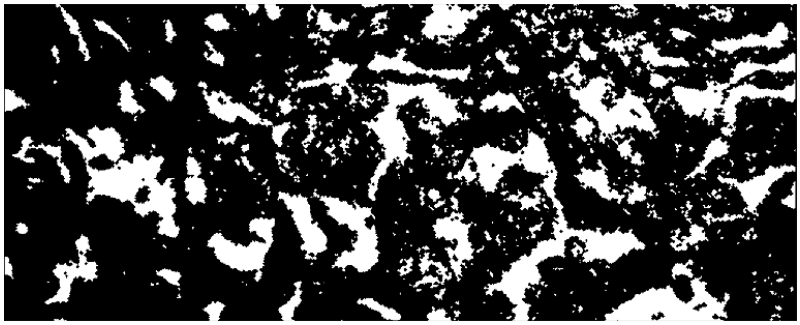

(b) Image after Opening operation

Figure 2.11: Influence of opening operation in segmentation of the cornea image

Using a sequence of closing followed by opening operations in morphological image processing, known as ”closing-then-opening,” can yield robust results by addressing different aspects of image preprocessing and enhancing the segmentation process. Initiating with closing helps remove small-scale noise and irregularities from the image. This maintains the objects' overall structure while preparing the image for subsequent processing steps by providing a cleaner and more stable starting point. After closing, applying an opening operation can further enhance object features and sharpen boundaries. This refinement process maintains the structural details while ensuring smoother and well-defined edges. The closing-then-opening sequence also mitigates the risk of over-smoothing since the latter eliminates the excessive smoothing introduced by the former.

It is worth saying that using opening followed by closing would produce the same results since they are reverse operations.

Removal of small holes and objects

The conventional segmentation method's last step is removing small holes (zeros) and objects (ones). This straightforward method depends on two factors: the threshold area to eliminate the smaller objects/holes and the connectivity that defines the relation between pixels.

The threshold area is the parameter that defines the boundary where a region or hole is removed or kept. Above a thousand pixels, the operation eliminates regions that can be considered keratocytes, so keeping this parameter in the order of hundreds of units is recommended. Pixel connectivity (Figure 2.12) is crucial when using the ”remove holes” function since it defines the establishment of boundaries of objects and components of regions in an image. Two pixels are said to be connected if they are adjacent in some sense(neighbour pixels,4/8/m-adjacency).

- **4-connectivity:** Two or more pixels are 4-connected if they are cardinal neighbours (above, below, to the left, or the right of the central pixel). It is the simplest, most efficient and least noise-sensitive implementation.

- **8-connectivity:** Two or more pixels are 8-connected if they are cardinal neighbours (top, bottom, left, and right) or diagonal neighbours, creating a diamond pattern around the central pixel. This implementation allows smoother borders and more continuous and detailed regions as it considers all peripheral pixels as neighbours.

- **m-connectivity:** This is a general case where the user can specify any positive integer value m greater than or equal to 1 based on a chosen connectivity pattern. These neighbours can be in various directions, depending on the specific definition. It is beneficial for data with specific characteristics as a custom connectivity type.

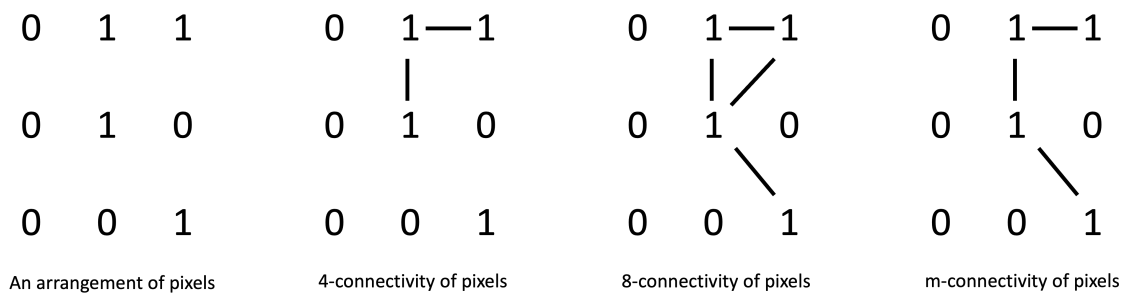

Figure 2.12: Different types of connectivity. Taken from [11]

For the available data we have, we tested 4-connectivity and 8-connectivity. Figure 2.13 shows removing holes and objects using 4-connectivity and a threshold area of 600 pixels. We can see that the operation is imperfect, allowing small regions to appear in the final image.

On the other hand, Figure 2.14 shows the improvement in eliminating small regions when using 8-connectivity with the same threshold area. Despite the improvement, the operation is still limited and cannot wholly remove holes and small regions, showing the computational limitations of this type of segmentation.

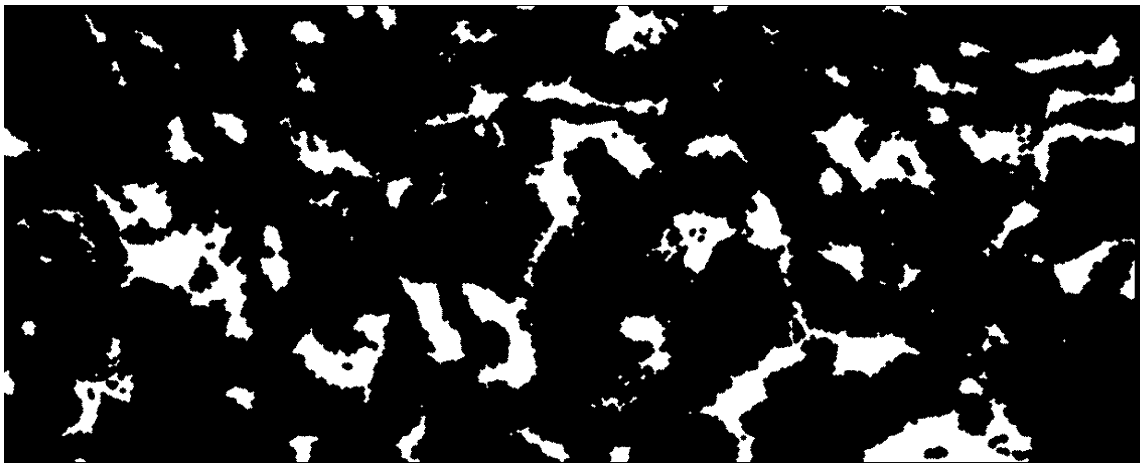

Figure 2.13: Removal of holes and objects using a 4-connectivity

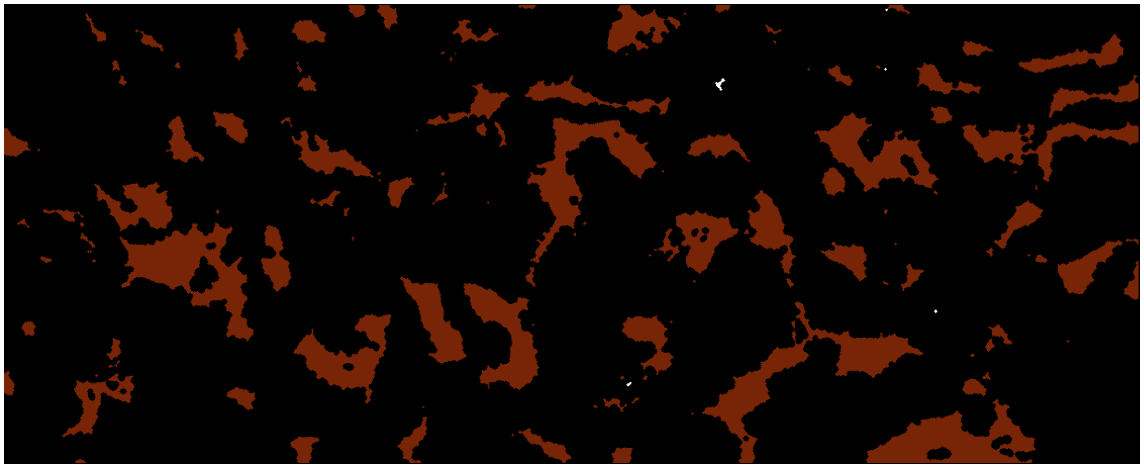

Figure 2.14: Removal of holes and objects using an 8-connectivity. The red regions represent the image after removing holes and objects using an 8-connectivity

Optimal combination of free parameters

Upon delving into the stages of the segmentation method, a noteworthy aspect comes to light: the existence of a free parameter in each operation dictating the outcomes of each operation. Therefore, finding the optimal combination is imperative for the most accurate results.

The cornea utilised in this study was a fixed-cornea, as it was the readily available option at the time. This choice ultimately proved advantageous for the study, as the smaller size and consistent high contrast provided by this dataset greatly facilitated the analysis and decreased the running time of the code. The investigation employed a conventional segmentation workflow, employing a set of combinations. Specifically, a range of values was explored: closing and opening disk radius parameters were examined within [1, 3, 5, 7, 9] pixels length, while the area threshold for removing holes/objects spanned [100, 200, 300, 400, 500, 600, 700, 800, 900, 1000] pixels size. Moreover, the Otsu threshold was multiplied by a constant, ”alpha”, varying across [0.5, 0.75, 1, 1.25, 1.5, 1.75, 2]. By

multiplying it with a constant, we aimed to determine whether the threshold value could be optimized, considering the intrinsic non-bimodal nature of the pixel distribution in the original image.

Figure 2.15 shows a parallel plot with the different types of combinations and their respective accuracy. The accuracy (2.7) is determined by assessing the segmented image against a manually annotated image.

$$F1 = \frac{2 \cdot TP}{2 \cdot TP + FP + FN} \tag{2.7}$$

Where:

- TP (True Positives) represents the number of correctly predicted positive instances.
- TN (True Negatives) represents the number of correctly predicted negative instances.
- FP (False Positives) represents the number of incorrectly predicted positive instances.
- FN (False Negatives) represents the number of incorrectly predicted negative instances.

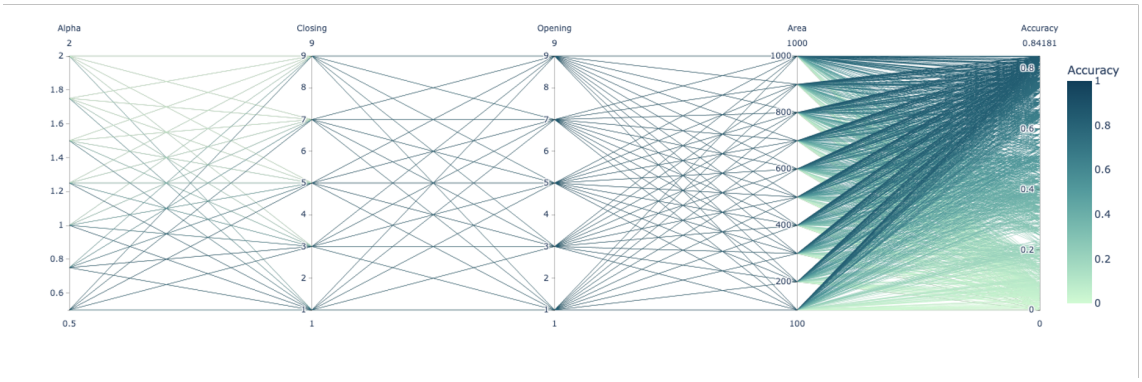

Figure 2.15: Parallel plot with 1750 combinations and respective accuracy

As anticipated, certain combinations yield high accuracy, while others result in intermediate or nearly zero accuracy. This underlines the necessity of identifying the optimized combination for each image, as diverse corneas may exhibit distinct characteristics. This divergence becomes particularly prominent in two situations: when comparing healthy corneas with diseased counterparts or considering different corneal states, such as fixed or non-fixed, and the disparity in resolution across various OCT machines. The problem with this search is that it could be more computationally efficient, and it is always necessary to have annotations made by experts in the field to compare the quality of the segmentation. In the case study, the running time was 23 hours and could be longer if the images used were larger. One solution would be to conduct a regression analysis and check the parameters with the most influence on the final result. This way, one could focus on exploring combinations involving those parameters, reducing the search space for parameter tuning and, consequently, the computational cost.

Table 2.3: Regression Analysis of Conventional Segmentation Parameters

params	coef	std err	t	P>|t|	[0.025	0.975]
const	0.6846	0.003	201.432	0.000	0.678	0.691
Alpha	0.0944	0.002	56.863	0.000	0.091	0.098
Closing	0.0096	0.000	33.721	0.000	0.009	0.010
Opening	-0.0018	0.000	-6.294	0.000	-0.002	-0.001
Area Threshold	2.38e-05	2.75e-06	8.658	0.000	1.84e-05	2.92e-05

The estimated coefficients shown in Table 2.3 provide essential insights into the significance of each variable. The high t-values and low p-values underscore the statistical significance of the test, and the coefficients show that all of the variables are influential in the model. As expected, the ”Alpha” coefficient is the most influential in the process since it is the segmentation’s first step and defines the initial quantity of black and white pixels. It is then followed by the ”Closing”, ”Opening”, and ”Area” coefficients, respectively. The area threshold coefficient reflects the relatively minor impact of this particular step on the outcome, primarily serving as a refinement in the final image. Regression analysis further substantiated that each successive step exerts a progressively smaller influence, as one would anticipate. This stems from the fact that with each iteration, the image converges closer to its original form, thereby diminishing the margin for adjustment in subsequent stages.

In our forthcoming comparative analyses, a specific combination for this segmentation type will be employed, effectively streamlining the algorithm’s runtime to 20 to 30 minutes. The selected combination, characterized by intermediate parameter values—alpha=1, closing=3, opening=5, and area threshold=600—demonstrated an accuracy rate of 85% when applied to the reference image.

2.2.2 Conventional Segmentation - Results

Once the construction of the workflow for morphological segmentation was completed, the method was applied to the images obtained during the internship. Figure 2.16 illustrates the accuracy achieved for each image.

As expected, the fixed cornea exhibited the highest accuracy (Figure 2.17) due to its high contrast, while the non-fixed corneas (Figure 2.18) ranged from 65% to 78%. The average accuracy of 72% represents a reasonable value and demonstrates the utility of this method in keratocyte segmentation. However, the accuracy variability highlights the method’s sensitivity to lower-quality datasets (in terms of contrast), thereby restricting its consistent use in a medical context.

In summary, while conventional segmentation effectively isolates keratocytes within the cornea, achieving optimal results requires significant time in parameter tuning. Moreover, a fundamental limitation of this method lies in its 2D nature, as it evaluates each

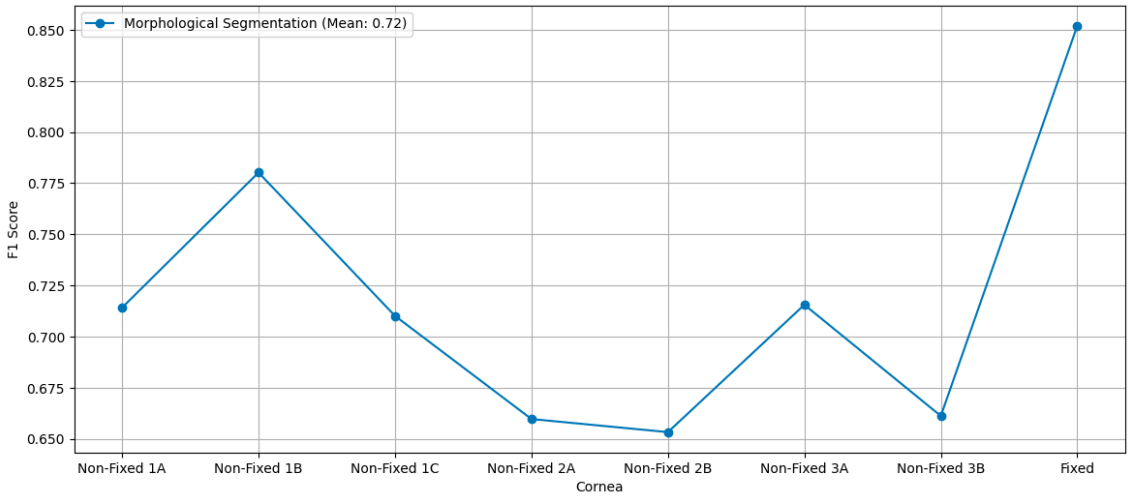

Figure 2.16: Conventional Segmentation Accuracy

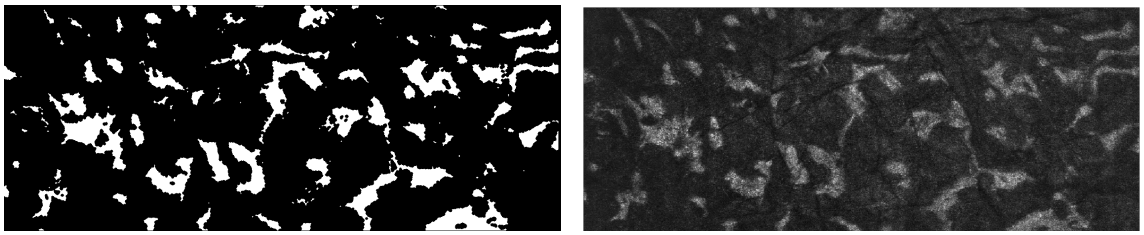

(a) Segmented Image (b) Original Image

Figure 2.17: Segmentation of fixed cornea

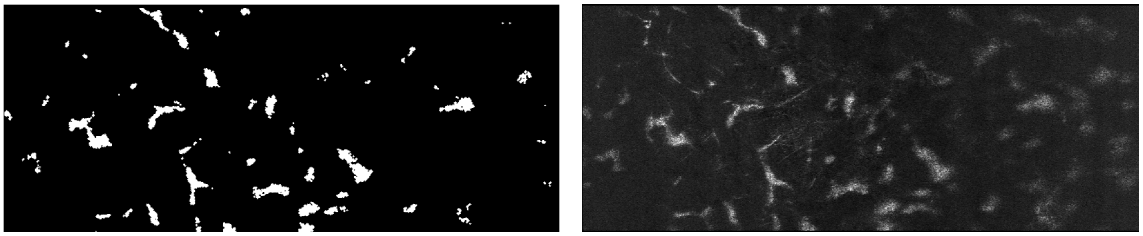

(a) Segmented Image (b) Original Image

Figure 2.18: Segmentation of a non-fixed cornea 1A

plane independently and disregards the intricate 3D arrangement of keratocytes. Given the thickness and potential interconnections between these cells, there is a need for an approach that accurately captures their 3D organization. Consequently, 3D segmentation techniques become crucial to overcome this limitation and ensure a comprehensive representation, enabling a more thorough analysis and preventing potential omissions, especially at the tips or extremities of elongated cells.

2.2.3 Deep Learning approach to image segmentation

How do we accurately examine and understand the complex three-dimensional architecture of keratocytes within the cornea? What innovative techniques consistently recognize

these cell patterns and, with a low running time, segment them? In recent years, medical image analysis has suffered a transformation, primarily driven by advancements in deep learning techniques. These procedures often induce better accuracy, efficiency and consistency due to the higher perception of patterns in the whole datasets. The 3DUNET [4] (3D U-Net) framework, a highly used architecture for biological tissue imaging, is a compelling option to answer these questions, offering a pathway to unlock a deeper understanding of corneal 3D structures by only requiring 2D annotated slices for training. Unlike traditional 2D neural networks, it considers the depth (z-axis) alongside the usual width (x-axis) and height (y-axis). 3DUNET inherits the highly effective U-Net architecture. This design features both an encoder and a decoder connected by skip connections. These skip connections simultaneously capture local and global features while preserving spatial information.

Convolutional Neural Networks fundamentals

In this subsection, we will delve into the fundamental concepts of neural networks, providing a foundational understanding that will aid in comprehending the 3DUNET architecture. Neural networks are a fundamental tool in machine learning, enabling computers to learn tasks by analyzing labelled training examples. The human brain inspires these networks that consist of numerous interconnected processing nodes.

In today's neural networks, nodes are organized into layers, creating a feed-forward structure where data flows in one direction. In the training phase, all weights and thresholds start with random values. Training data is inputted, passes through the layers, and the network continually adjusts the weights and thresholds until it consistently produces desired outputs for labelled training examples.

Layers act as building blocks for processing and feature extraction from data. In 3DUNET, 3D convolutional layers are central to the hidden layers. Convolutional layers extract local spatial features from three-dimensional input data. The typical steps of the convolutional layer are:

- **Convolution Operation:** The convolutional layer performs the convolution mathematical operation by taking a small filter (also known as a kernel) and sliding it over the input data systematically. The filter is a 3D matrix with learnable parameters.
- **Local Feature Extraction:** As the filter slides over the input data, it computes the element-wise dot product between the filter and a local region of the input. This dot product summarizes certain features or patterns within that region. The result is a single value in the output feature map.
- **Strides:** During convolution, the filter moves across the input data with a specified step size known as the ”stride.” The stride determines how much the filter shifts in each step. A larger stride results in a smaller output feature map as it skips over

input regions.

- **Padding:** Padding is an optional technique that involves adding additional pixels around the input data. Padding can be ”valid” (no padding) or ”same” (padding added to keep the output dimensions the same as the input). Padding helps control the spatial dimensions of the output feature map.
- **Activation Function:** After the convolution operation, an activation function is typically applied element-wise to each value in the output feature map. Activation functions introduce non-linearity into the network's computations. They determine whether a neuron should activate based on the computed weighted sum of its inputs. This process occurs layer by layer, enabling the network to capture complex patterns and relationships in data. In the 3DUNET, the chosen activation function was the Rectified Linear Unit (ReLU) due to its simplicity and effectiveness. In ReLu, a neuron is activated if the weighted sum of its inputs is higher than zero:

$$f(x) = \max(0, x) \tag{2.8}$$

- **Output Feature Map:** The result of the convolution operation and the application of the activation function is an output feature map. This feature map represents the presence of different features at different locations within the input data.
- **Pooling:** A pooling layer may follow the convolutional layer. A pooling layer, max pooling in the 3DUNET, reduces the spatial dimensions of the feature map. Within each kernel, max pooling identifies and retains the maximum value and discards the rest. In essence, it captures the most prominent feature within that window, helping to reduce computational complexity and focus on essential features.

$$MaxPooling(x, y) = \max(x, y) \tag{2.9}$$

Hidden layers in 3DUNET encompass an encoder-decoder structure inspired by U-Net, incorporating convolutional and deconvolutional layers. The encoder part of the network, which usually comes first, uses convolutional layers to progressively downsample the input data, extracting hierarchical, local features and patterns. The decoder part of the network, which follows the encoder, uses deconvolutional layers to upsample and reconstruct the segmented output. This part also incorporates skip connections to maintain fine-grained spatial information, contributing to accurate segmentation. These connections directly connect layers in the encoder to corresponding layers in the decoder.

In summary, the hidden layers in 3DUNET encompass encoder and decoder layers, skip connections, activation functions, and normalization layers. These elements collaboratively process and transform the input volumetric data, capturing spatial features and patterns in three dimensions to facilitate accurate 3D segmentation.

3DUNET architecture

This subsection will comprehensively explore the 3DUNET architecture (Figure 2.19).

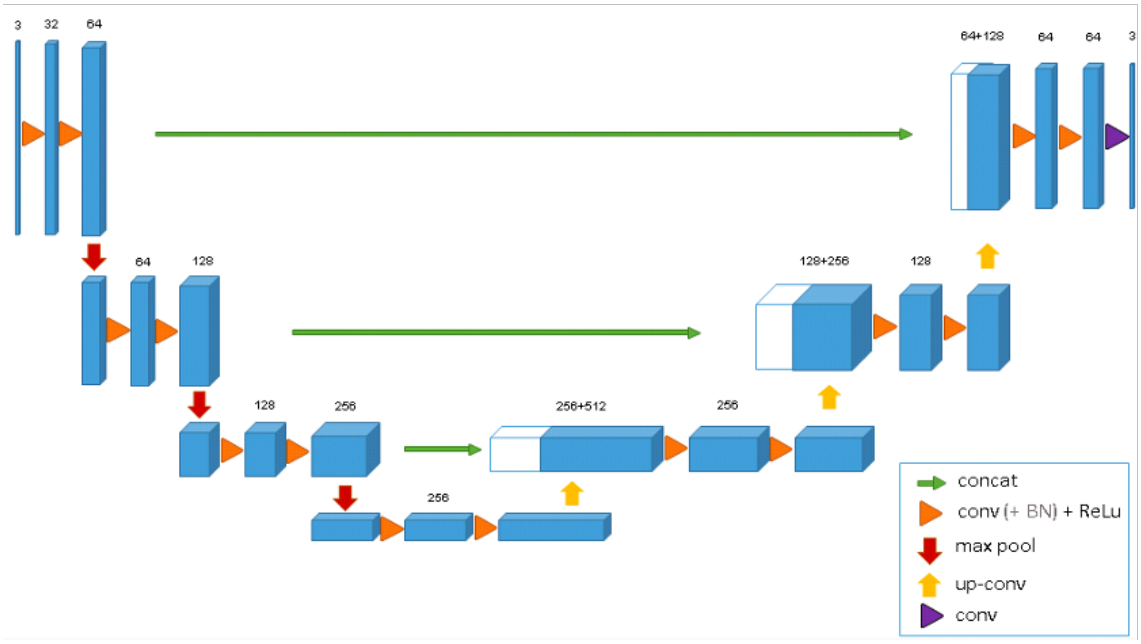

Figure 2.19: 3D U-NET Architecture. Taken from [4]

As previously mentioned, 3DUNET has an encoder and decoder structure with the following specifications:

- **Encoder-Decoder Structure:**
  - Resolution Steps: Each path consists of four resolution steps. In the analysis path, each layer employs two 3 × 3 × 3 convolutions, each followed by a rectified linear unit (ReLU) and a subsequent 2 × 2 × 2 max-pooling operation. The synthesis path includes up convolutions of 2 × 2 × 2 and two 3 × 3 × 3 convolutions followed by a ReLU.
- **Shortcut Connections:**
  - High-Resolution Features: Shortcut connections link layers of equal resolution in the analysis and synthesis paths.
- **Final Layer and Parameters:**
  - Final Layer: In the final layer, a 1 × 1 × 1 convolution reduces the number of output channels to match the number of labels, typically three for keratocyte segmentation.
  - Parameter Count: The entire 3DUNET architecture comprises approximately 19,069,955 parameters, making it a robust and expressive network.
- **Input and Output:**
  - Input: The network's input consists of a 132 × 132 × 116 voxel (3D pixel) tile of the image, with three channels, providing a comprehensive data view.

  - Output: The final layer's output consists of 44 × 44 × 28 voxels in the x, y, and z dimensions, respectively. This configuration ensures that each output voxel can access sufficient contextual information for efficient learning.

- **Weighted Softmax Loss Function:**
  - Sparse Annotations: The network leverages a weighted softmax loss function, where the weights of unlabeled pixels are set to zero. This allows the network to learn exclusively from the labelled pixels, promoting effective generalization to the entire volumetric image.

Training specifications

The 3DUNET gives the user freedom regarding the loss function and initial parameters so that we can adequate the training setup for our specific case. The specifications of the training sessions used are:

- **Initial Number of Feature Maps:** 32

  This parameter determines the number of feature maps in the initial layers of the model. Feature maps are the channels in the convolutional layers.

- **Number of Groups in GroupNorm:** 8

  Group Normalization is a technique to stabilize training by normalizing group feature maps.

- **Loss Function:** BCE-Dice Loss (Binary Cross-Entropy + Dice Loss)

  Among the available options, the loss function used is BCE-Dice Loss, a combination of Binary Cross-Entropy (BCE) and Dice Loss. BCE measures the dissimilarity between predicted and ground truth masks, while Dice Loss measures the overlap between predicted and ground truth masks. Combining these two loss functions gives the best result in segmentation, pixel-wise accuracy and generalization [17].

  Equation 2.10 represents the BCE Loss as a function of the predicted values x and the true labels y:

$$BCELoss(x, y) = -\frac{1}{n}\sum_{i=1}^{n}(y_i \log(x_i) + (1 - y_i)\log(1 - x_i)) \tag{2.10}$$

  Equation 2.11 represents the Dice Loss as a function of individual true labels (ground truth) for each element i, y_i, and individual predicted values (probabilities) for each element i,p_i.

$$DiceLoss = \frac{2 \cdot \sum_{i=1}^{n} y_i \cdot p_i}{\sum_{i=1}^{n} y_i^2 + \sum_{i=1}^{n} p_i^2} \tag{2.11}$$

- **Initial Learning Rate:** 2×10^{-4}

The initial learning rate is a hyperparameter that controls the step size during gradient descent optimization. The range of values to consider for the learning rate is less than 1.0 and greater than 10^{-6}. The value of 2×10^{-4} indicates a relatively low learning rate, standard for similar deep learning models.

- **Maximum Number of Epochs per training session:** 1000

  This parameter sets the maximum number of training epochs. An epoch represents one complete pass through the training dataset. Early stopping may halt training if the model's performance plateaus.

- **Patch Size for Input:** (32, 64, 64) for non-fixed and (16, 32, 32) for fixed cornea.

  The patch size defines the spatial dimensions of the input data that the model processes. In this case, the model processes 3D input data in size patches (32, 64, 64).

- **Stride Size:** (32, 64, 64) for non-fixed and (16, 32, 32) for fixed cornea.

  The stride size determines the step size at which the model moves the processing window (patch) across the input data. The model processes non-overlapping patches with a stride of (32, 64, 64).

- **Training phases:**

  The datasets consist of cubes of different sizes: 200 pixels for non-fixed corneas and 100 pixels for fixed corneas. This difference occurred because the fixed cornea annotation was already available, and non-fixed cornea datasets present a lower contrast, so a bigger annotation was made to facilitate the comprehension of patterns by the model. The training dataset corresponds to 70% of the cube in-depth, and the validation dataset corresponds to 30% of the cube in depth. Validation was performed after every 1000 iterations during training. To evaluate the effectiveness and accuracy of the 3DUNET architecture, we conducted a series of four progressive training sessions:

  - The first training phase covered iterations from 0 to 53,000.
  - The second phase covered iterations from 53,000 to 103,000.
  - The third phase covered iterations from 103,000 to 151,000.
  - The final phase covered iterations from 151,000 to 300,000.

  The four progressive training sessions utilized diverse datasets extracted from four distinct corneas, one fixed and three non-fixed. This approach optimizes the model's adaptability to corneas at different conditions and corneas with temporal variations since non-fixed corneas, undergoing deswelling processes, exhibit dynamic changes over time, yielding unique variations for each image captured from the same cornea at distinct time points. This variability proves invaluable for training machine learning

models, as it allows for generating diverse datasets with minimal material requirements in case we want to perform more training sessions.

2.2.4 Deep Learning - Training and Testing results

Training Performance

The training performance of a neural network can be assessed by considering five key parameters: Learning Rate (Figure 2.20), Training Loss Average (Figure 2.21), Training Evaluation Score (Figure 2.22), Validation Loss (Figure 2.23), and Validation Evaluation Score (Figure 2.24).

The learning rate periodically decreases without abrupt increases, demonstrating the stability of the training process and its ability to generalise effectively to training and unseen validation data.

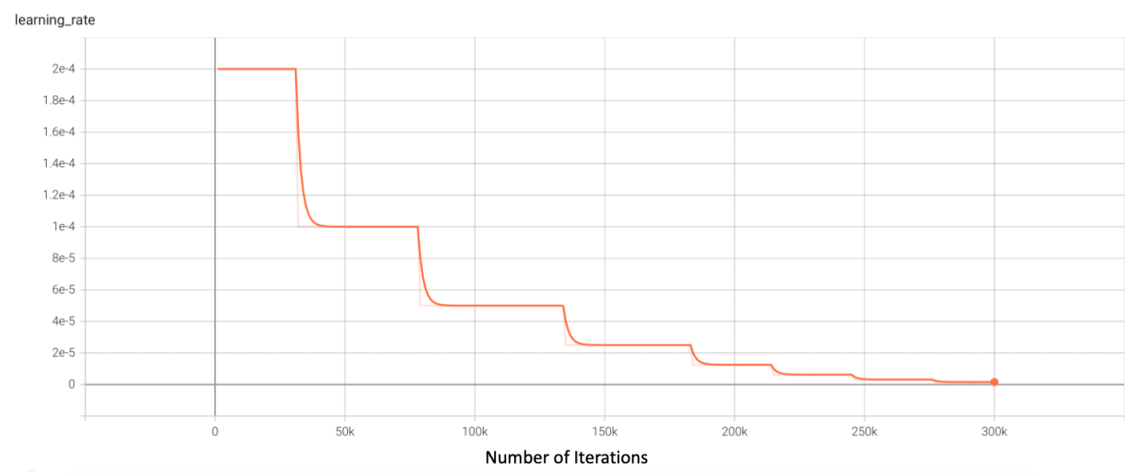

Figure 2.20: Training Learning Rate

The training loss gradually decreases over training, signifying the model's learning process and convergence towards an optimal solution. However, it is noteworthy that temporary fluctuations in the loss are observed at the onset of each new training phase. These fluctuations are anticipated as the training metrics adapt to the distinctive characteristics of the new dataset. Concurrently, the model's hyperparameters and weights adjust to attain new optimal values tailored to the dataset's specific attributes.

On the other hand, the training evaluation score quantifies how well the model fits the training dataset. The steady improvement over iterations indicates that the model successfully captures complex patterns in the training data. It is also worth noting that both metrics follow the inverse behaviour through the iterations during the first three training phases, showing that the model is not overfitting during training. In the last training phase, both started to flat, an indicator of possible overfitting, which is why no more training sessions were done.

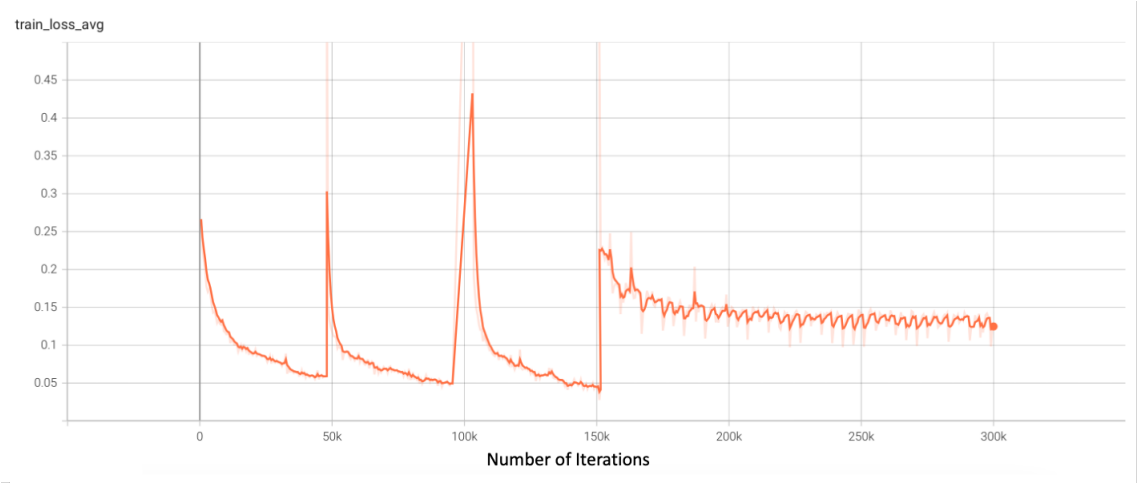

Figure 2.21: Average Training Loss

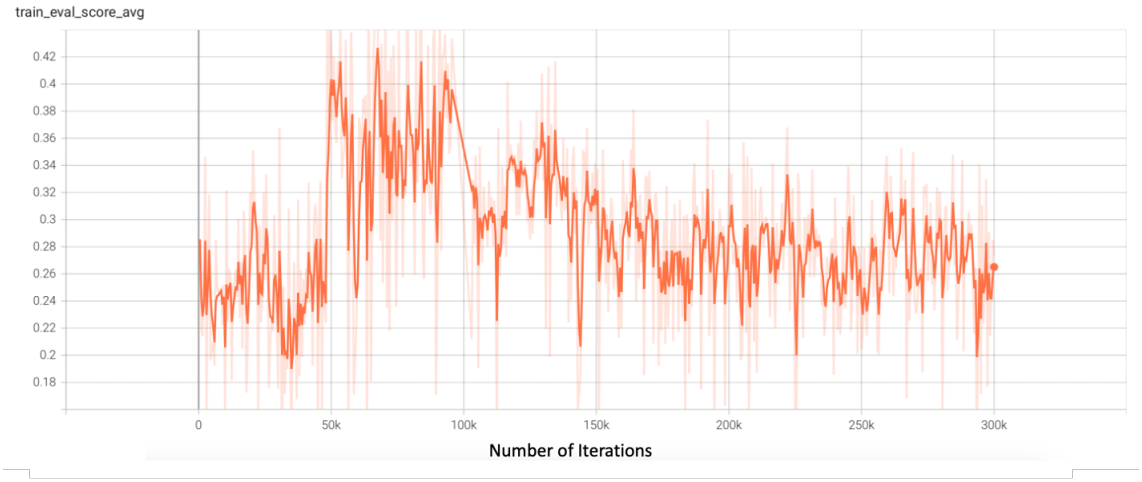

Figure 2.22: Average Training Evaluation Score

During the validation phase, the evaluation loss experienced a subtle decline during the initial three training sessions due to the similarities of the datasets (non-fixed corneas) since the model is not learning much. The model's learning progress in this phase was relatively limited. .A drop was observed in the last training session, which marked a transition to a dataset with distinct characteristics (fixed cornea). The reduced evaluation loss implies an improved ability to make predictions that closely align with the ground truth.

Unlike the evaluation loss, the validation evaluation score exhibited a consistent increase. The upward trajectory of the validation evaluation score indicates a continuous enhancement in the model's ability to generalize its learnings to previously unseen data. As the model adapts to new information and variations, its capacity to make accurate predictions improves, resulting in higher validation evaluation scores. The interplay between validation loss and validation evaluation score underscores the model's generalization and adaptability.

In conclusion, the training phase stands as a resounding success. The observed

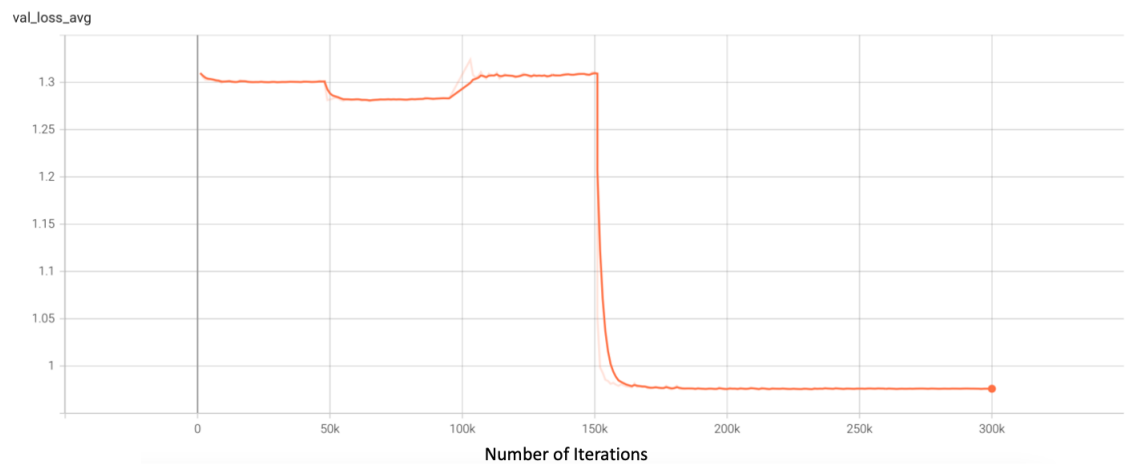

Figure 2.23: Average Validation Loss

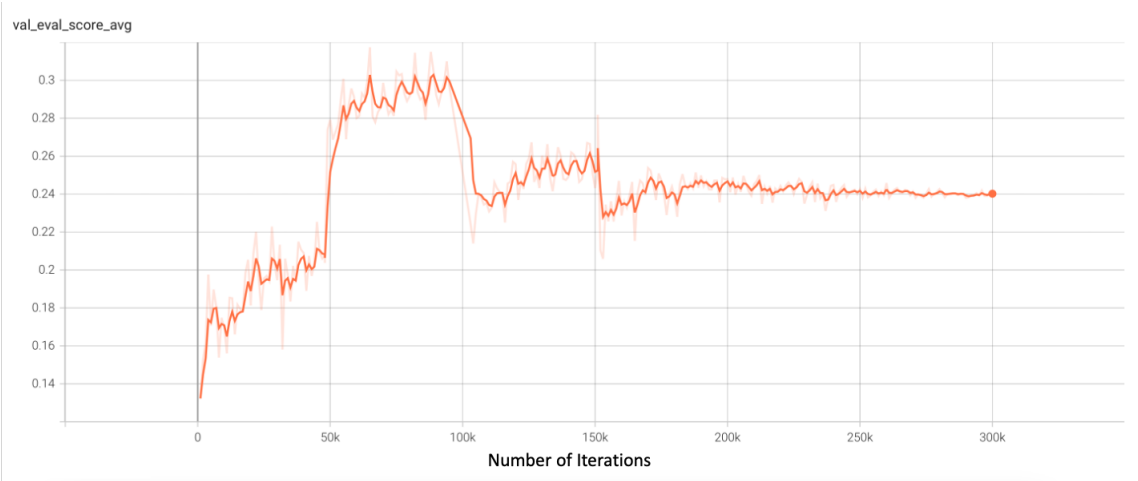

Figure 2.24: Average Validation Evaluation Score

trends in key metrics demonstrate the model's ability to adapt, learn, and generalize effectively.

Testing Phase

After training the 3DUNET model for segmentation, the next phase, testing, evaluates its performance on untrained data by observing its segmentation predictions. The output of the 3DUNET model, during both training and testing, is a probability map (Figure 2.25a). This probability map represents the likelihood of each pixel in the input OCT image belonging to a segmented region (white region). While a probability map is informative, practical applications require a binary segmentation map. A thresholding step is necessary to convert the probability map into a binary image (Figure 2.25b). It involves selecting a threshold value, between 0 and 1, above which pixel values are considered part of the keratocyte and below which are not.

The choice of the threshold value can significantly impact the quality of the binary seg-

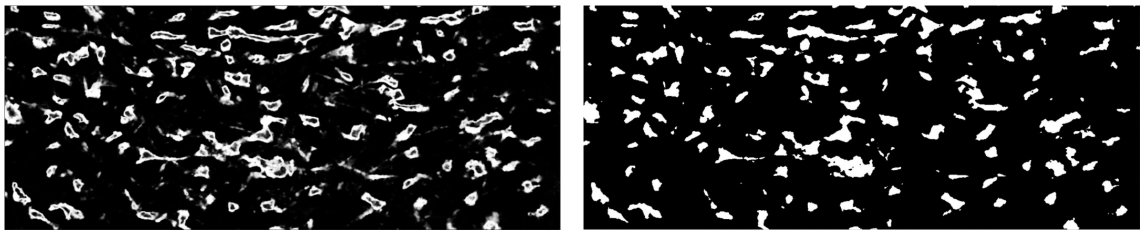

(a) Probability map (b) Binary image

Figure 2.25: Transformation of 3DUNET probability map to binary segmented image

mentation. An appropriate threshold value depends on factors such as the characteristics of the dataset, the specific application, and the desired trade-off between sensitivity and specificity. Different threshold values were used during the testing phase, and the segmented image was compared to the corresponding annotation. Among these values, 0.7 consistently emerged as the threshold, providing the highest F1 score (eq.2.7). Consequently, this threshold value was chosen for further analysis.

Segmentation Results

The results (Figure 2.26) indicate that the 3D U-Net model consistently outperforms conventional segmentation methods across various corneas in different states. Its adaptability and capacity to capture fine details contribute to its superior performance, especially when dealing with challenging cases such as noisy data or low-contrast images.

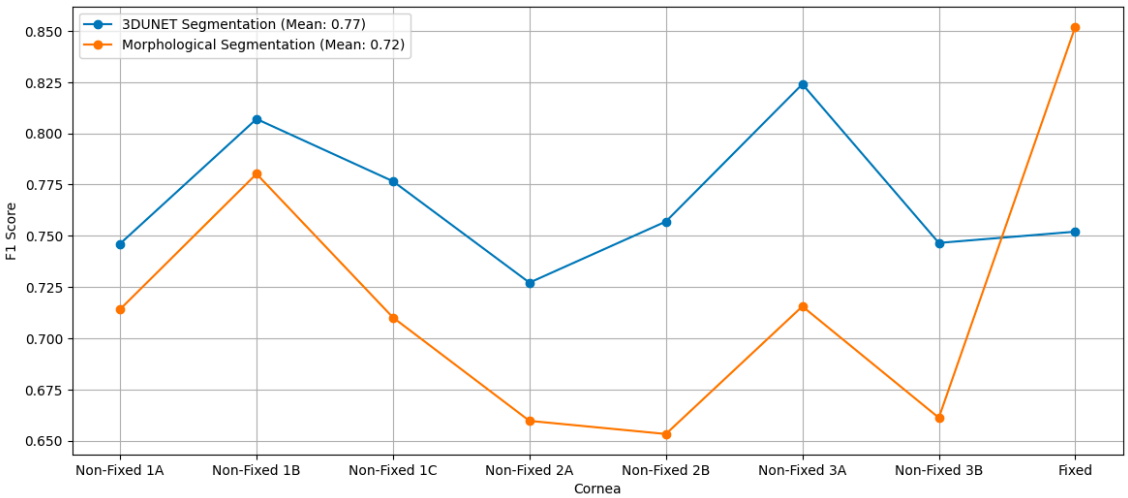

Figure 2.26: 3DUNET vs Conventional segmentation accuracy

The possibility of doing more training sessions with datasets of corneas in more exotic states (diseased corneas) shows the potential of this new methodology to enhance the reliability of anatomical structure segmentation, benefiting clinical diagnosis, treatment planning, and medical research. This method offers another notable advantage in terms of its rapid testing phase. Despite each training session requiring approximately 7 hours, once

the final model is in place, the testing process is remarkably efficient, completing in just 20 to 30 minutes. Moreover, this testing phase delivers segmented images with accuracies exceeding 77%. Achieving such a level of accuracy with conventional methods would necessitate a parameter tuning process, which is considerably more time-consuming than the testing phase in 3DUNET.

Moreover, Figure 2.27 shows the original and segmented images at a determined depth. When navigating through the peripheric planes at that specific depth, it is possible to see an increasingly whiter region in the lateral part, showing that those regions are indeed keratocytes. Despite the low contrast, the 3DUNET method detected these regions as keratocytes correctly. In contrast, the conventional method exhibited inefficiency in detecting these features in the same conditions.

Figure 2.27 serves as a visual testament to the 3DUNET method's capacity to discern finer details and structures within the corneal images, particularly when faced with challenging contrast conditions.

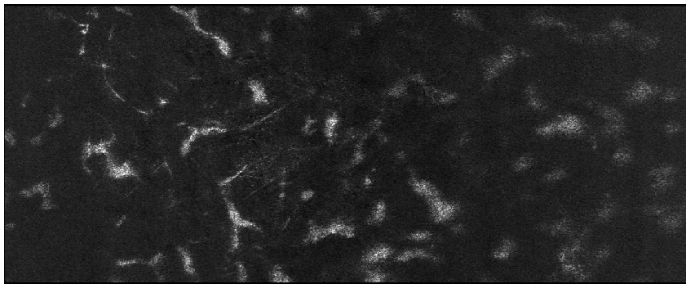

(a) Original image of non-fixed cornea

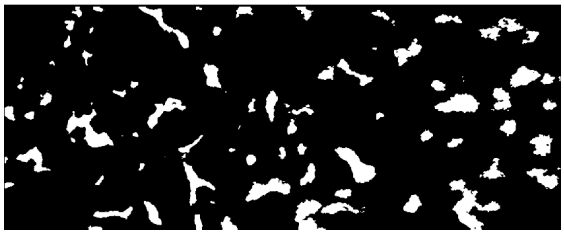

(b) 3DUNET segmented image

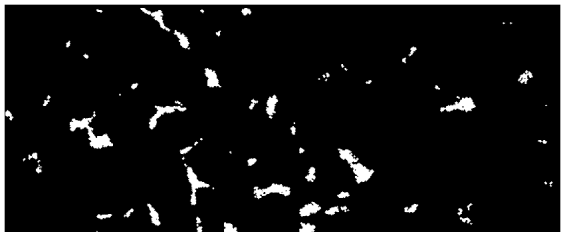

(c) Morphologically segmented image

Figure 2.27: Differences between original and segmented images from 3DUNET and conventional methods.

2.2.5 Conclusion

This chapter provided a comprehensive comparison between two segmentation methods: conventional segmentation and deep learning architecture, 3DUNET. The following table (Table 2.4) outlines the key advantages and disadvantages associated with each technique.

In conclusion, the comparison underscores the promising potential of 3DUNET as a cutting-edge tool for image segmentation tasks, particularly in scenarios where speed

Table 2.4: 3DUNET vs Conventional segmentation

Aspect	Conventional Segmentation	3DUNET
Advantages		
Precision	-Well-understood, interpretable algorithms; -Good performance in some scenarios.	-Potential for high levels of accuracy due to deep feature learning; -Adaptability to complex patterns and structures.
Flexibility	-Customizable with domain-specific rules; -Applicable to a wide range of tasks.	-Versatile and applicable to diverse medical imaging tasks; -Can handle variations in data, structures, and modalities.
Disadvantages		
Generalization	-May struggle with complex structures, noise, or data variations; -Requires extensive feature tunning.	-Dependency on large labelled datasets for effective training; -It may not perform well on rare or novel conditions.
Training Data Requirements	-Less data-hungry; may perform reasonably well with smaller datasets.	-Requires large amounts of annotated data for effective training.
Computational Resources	-Typically, less computationally intensive; -It can be deployed on resource-limited hardware, making it suitable for modest clinical environments	-It demands significant computational power and memory, often requiring GPUs or specialized hardware.

and high accuracy are paramount. Nevertheless, the choice between conventional segmentation and 3DUNET should be made judiciously, considering the specific needs and constraints of the given application. However, it is essential to carefully consider when choosing between conventional segmentation and 3DUNET, considering the unique requirements and limitations of the specific application. To further assess the practical implications of this choice, optical analysis will be conducted using the segmented images generated by both methods. This approach aims to scrutinize any discernible differences in the results produced by each method to achieve optimal results.

Chapter 3

Wavefront and Corneal Analysis

After a comprehensive understanding of the functioning of the OCT technique and the segmentation of its images through conventional and deep learning techniques, it is now possible to perform an optical analysis of the segmented images. Wavefront analysis has appeared as a critical domain within ocular imaging, facilitating a profound understanding of the optical characteristics of the eye. This section will provide a fundamental understanding of the most prominent methodologies and metrics for corneal transparency analysis and present preliminary results in the state of different corneas for further studies in cornea scattering. Here, the interest remains in small scattering angles near the unit, which can serve as a foundation for studies at higher scattering angles.

3.1 Keratocyte Volume

The initial step in our analysis involves comparing keratocyte volume in the stroma to validate the segmentation method's reliability and provide quality control when juxtaposed with theoretical values, primarily when corneal conditions are known. Moreover, it can offer valuable insights into the clinical state of the cornea when the current condition is not pre-established.

To calculate the volume fraction of keratocytes within the stromal volume, we determined the ratio of white pixels to the total number of pixels in each plane of the z-stack and then computed the overall mean volume fraction. This approach allows the identification of a possible evolution with depth of the keratocyte's volume fraction.

Table 3.1 presents the mean volume of keratocytes and their respective standard deviations. Since all corneas used in this study are healthy, keratocytes are expected to occupy approximately 10% of the total stromal volume. Notably, the results show that the obtained values in all the images are relatively close to this theoretical approximation, suggesting that our method yields realistic values. However, there is a clear difference between the two methods, with 3DUNET sometimes yielding double the percentage ob-

tained through the conventional method, except for the fixed cornea. This behaviour is expected, considering that the fixed cornea exhibits higher contrast, enhancing the accuracy of the conventional method and increasing the percentage of detected keratocytes. In contrast, non-fixed corneas tend to have lower contrast and generally darker regions, making keratocyte identification more challenging for the conventional method. On the other hand, 3DUNET consistently produces accurate results, showcasing its versatility for corneas in various conditions. In the subsequent wavefront analyses, the impact of these variations will be explored.

Table 3.1: Keratocytes Volume in Stroma

	3DUNET		**Conventional**	
Cornea	Mean	Std Dev	Mean	Std Dev
Non-fixed 3A	11.0	1.2	5.1	1.6
Non-fixed 3B	6.6	0.9	4.9	0.8
Non-fixed 3C	9.7	1.8	4.6	1.5
Fixed	11.8	1.9	13.8	3.5

Figures 3.1 and 3.2 illustrate the variation in the percentage of white pixels across each plane.

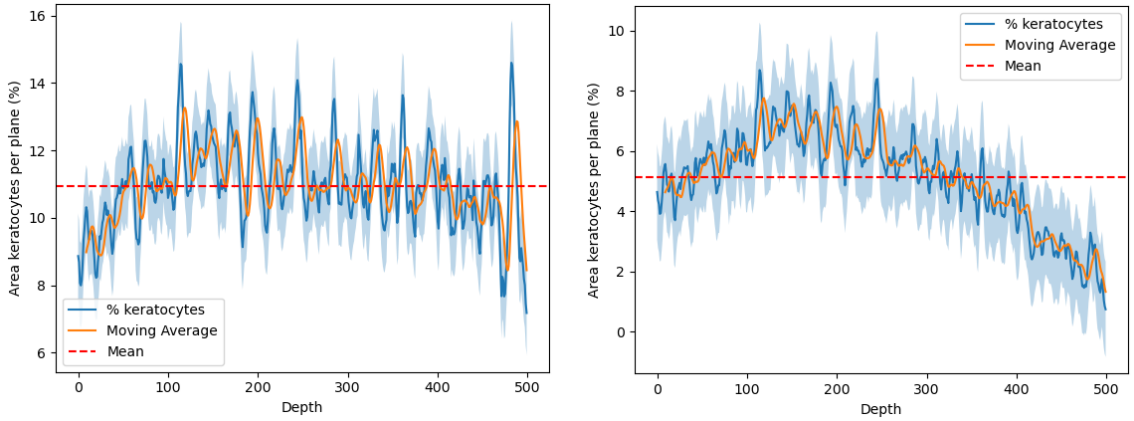

(a) Distribution of Keratocytes by plane in the 3DUNET segmented image

(b) Distribution of Keratocytes by plane in the conventionally segmented image.

Figure 3.1: Keratocyte Distribution on Non-Fixed Cornea 3C

The graphs show that the distributions do not follow a clear trend. Notably, at both the top and bottom of the stroma, we observe sudden and pronounced increases (Figure 3.2b) and declines (Figures 3.1b) in the percentage of keratocytes when segmentation is performed using the conventional method. This highlights the method's reduced efficiency in cases of low contrast and regions that are typically darker, even if these regions may still represent the initial or final portions of keratocytes (sudden decrease) or areas with a high proportion of white and intermediate pixels, which may inflate the count of segmented white pixels (sudden increase).

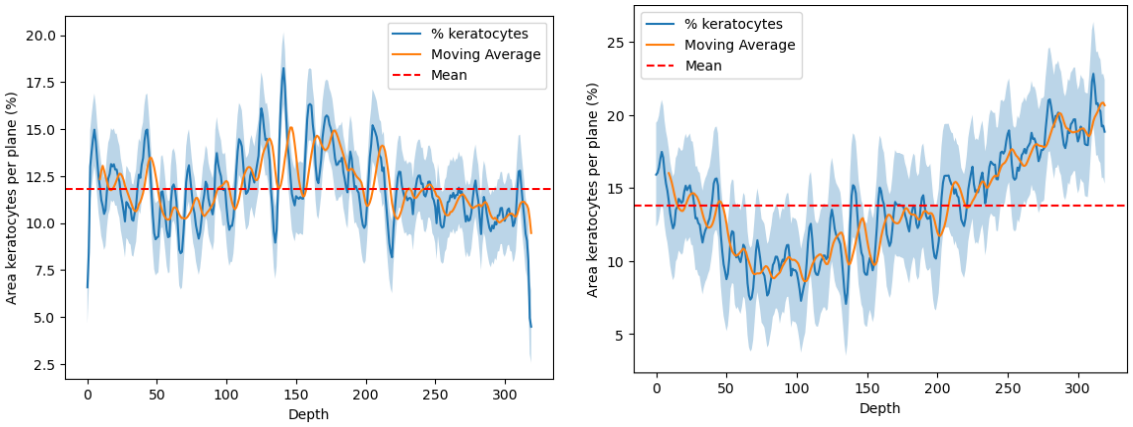

(a) Distribution of Keratocytes by plane in the 3DUNET segmented image.

(b) Distribution of Keratocytes by plane in the conventionally segmented image.

Figure 3.2: Keratocyte Distribution on Fixed Cornea

3.2 PSF

This section will involve the evaluation of the Point Spread Function (PSF) generated by each of the images. The workflow for this analysis can be divided into three distinct stages: image masking, Fourier Transform and PSF. Following this structured workflow enables systematically assessing and comparing the differences generated by each method on each step.

3.2.1 Image Masking

As light encounters the cornea, it may refract, scatter, or otherwise interact with its surface and structure. One approach to simplifying understanding the cornea's role as an obstacle to light is by considering single-scattering events. This allows the simplification of the image by doing a z-axis summation. The summation of pixel values along the z-axis collapses the three-dimensional volumetric data into a two-dimensional representation, emphasising these interactions and highlighting the cornea's role as a light-obstructing obstacle. Since the OCT images consider the reflection, it is necessary to invert the pixel value and then, due to the summation, correctly evaluate the white pixels as light passing through and black pixels as regions with obstacles where the light is strongly scattered or reflected.

However, it is essential to note that in OCT images, pixel values typically represent the degree of reflection, with white pixels corresponding to highly reflective surfaces, such as keratocytes, and black pixels indicating areas where light is less reflected or strongly scattered. To correctly evaluate the cornea as an obstacle to light, the first step is inverting the pixel values and then applying the z-axis summation.

Figure 3.3 illustrates the contrasting masks obtained from different images within a non-fixed cornea dataset. As anticipated, the mask derived from the original image ex-

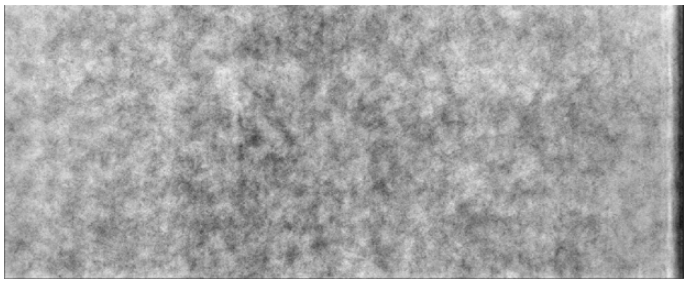

(a) Mask of the original image

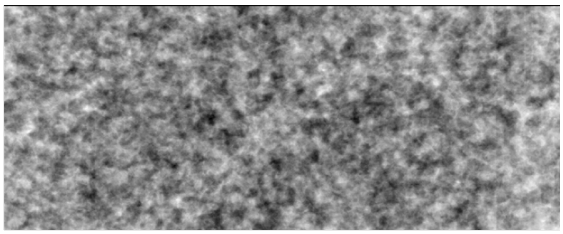

(b) 3DUNET Image Mask

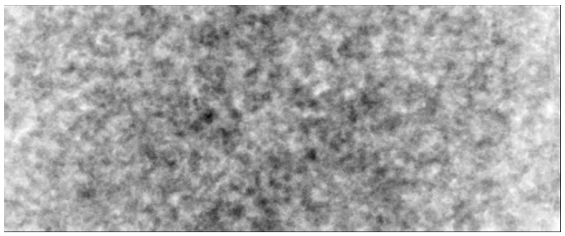

(c) Conventional Method Image Mask

Figure 3.3: Calculated masks for different segmented images

hibits a uniform distribution of values. This uniformity can be attributed to intermediary pixel values introduced by noise, resulting in a less distinct mask. The 3DUNET segmented image presents a mask with uniformly distributed black regions, highlighting the model's robust capacity to detect keratocytes in the lateral part of the images despite the lower contrast in these regions. In contrast, the conventional segmented image has similarities to the 3DUNET mask in the central region, with prominent black areas. However, on the lateral parts, the mask is whiter, showing the low efficiency of keratocyte detection in low-contrast images.

In summary, Figure 3.3 underscores the contrasting outcomes of different segmentation methods when applied to a non-fixed cornea dataset. It is anticipated that these disparities will continue to shape the outcomes within the workflow, ultimately impacting the accuracy, and insights gained from these analyses.

3.2.2 Fourier

Following the masking stage, the next step entails applying a Fourier transform to the mask. The Fourier transform will convert the spatial domain information of the image into the frequency domain.

Figure 3.4 illustrates the contrasting Fourier planes obtained through different methodologies. In all cases, the planes reveal a prominent bright spot at the centre, point (0,0), within the frequency domain. This point represents the zero-frequency or DC (Direct Current) component, indicating the uniform or average illumination level across the corneal image. However, distinct types of artefacts become apparent in these Fourier planes. In the case of the original image, vertical lines emanate from the centre, introducing a

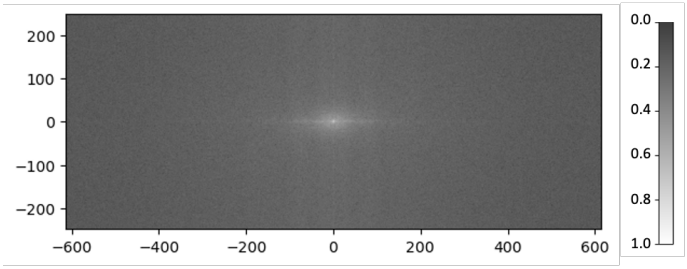

(a) 2D Fourier plane of the original image mask

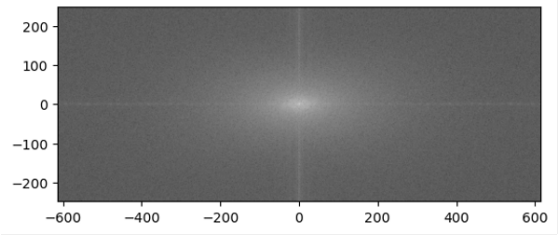

(b) 2D Fourier plane of the 3DUNET image mask.

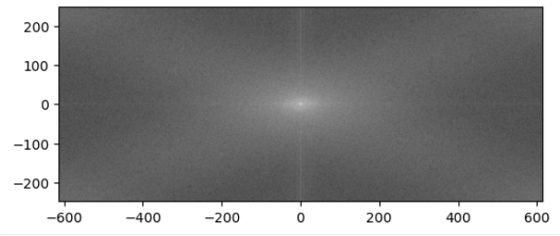

(c) 2D Fourier plane of the Conventional image mask.

Figure 3.4: Calculated 2D Fourier planes for masks

particular form of aberration into the frequency domain. The Fourier plane resulting from the 3DUNET segmented image exhibits a cross pattern centred at the (0,0) frequency point. Conversely, the Fourier plane produced by the conventional segmentation method displays a similar cross pattern as seen in the 3DUNET plane and a thick, faded diagonal cross.

This unexpected behaviour observed in the Fourier planes warrants a more comprehensive investigation in the acquisition and segmentation of the images to comprehend the eventual impact of these processes in the presence of artefacts. The Point Spread Function (PSF) production will be a critical aspect of this analysis to determine whether these artefacts alter the anticipated radial behaviours or remain consistent with the expected outcomes.

3.2.3 Radial PSF

In the final stage, the radial PSF of the Fourier-transformed image is produced. The radial PSF represents how the intensity of light from a point source is distributed in radial directions from that source. It provides valuable insights into the image's ability to resolve fine details and any aberrations or distortions that may be present.

Figure 3.5 illustrates the distinct PSF curves observed in two different non-fixed corneas. The PSF curves of the 3DUNET and Conventional images show similar behaviour with slight differences in higher scattering angles and peak intensity. The similarity between these curves can be attributed to the detection capabilities of both segmentation methods. The conventional method struggles to recognize smaller regions, such as the tails or tips

of keratocytes, sometimes leading to accuracy differences. However, these differences are mitigated by employing a mask that collapses the z-axis dimension.

In both corneas, the PSF curve of the original image displays lower intensities across most of the range of angles. This is also an expected behaviour consistent with the characteristics of original images, which often contain noise. The broader and less intense PSF curve of the original image indicates the refinement and feature enhancement achieved through segmentation. An interesting observation is how the curve of the original image begins to approach the values of the segmented images at the far end of the axis (-2º and 2º). This can be attributed to specific features or structures within the cornea that align with the segmentation process, resulting in localized intensity increases in these directions.

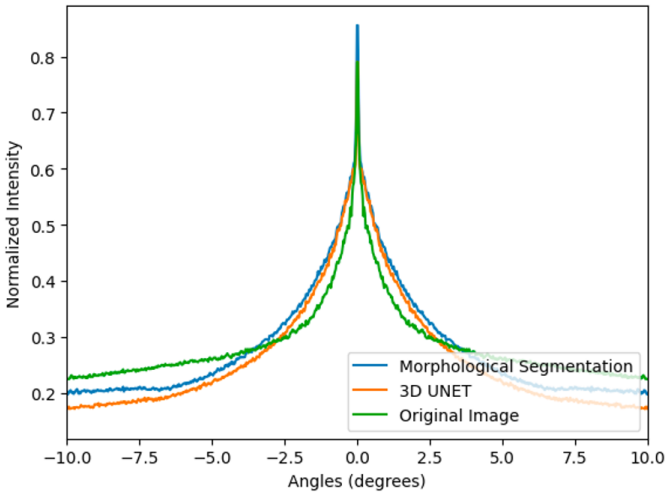

(a) Typical PSF obtained for the datasets available. In this example, it is represented the PSF of non-fixed cornea 1A.

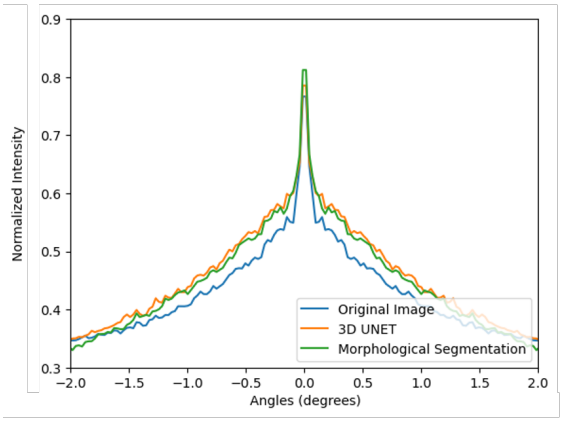

(b) PSF of non-fixed cornea 1A

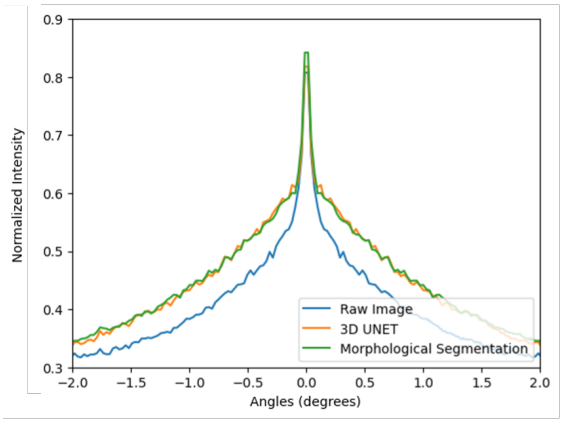

(c) PSF of non-fixed cornea 3C

Figure 3.5: Differences between PSF curves of two non-fixed corneas. The y-axis values were calculated using a log scale and normalised.

Figure 3.6 illustrates the contrasting PSF curves between a non-fixed and fixed cornea. The fixed cornea image corresponds to the dataset where the conventional method achieved higher accuracy (85%) than the 3DUNET method (75%). In this cornea, the curve of the

conventional method has a consistently lower intensity than the 3DUNET curve, a different behaviour than the non-fixed counterparts. A crucial insight comes from the distribution of keratocytes, as shown in Figure 3.2. This is the dataset with higher differences in the keratocyte distribution. The conventional segmentation method identifies a higher percentage (around 20%) of keratocytes in the deeper part of the stroma, leading to a mask with more black regions. In contrast, the 3DUNET method identifies a lower percentage (around 10%) of keratocytes in the same stromal region. Consequently, the mask generated by the 3DUNET method has fewer black regions. One would expect the PSF curve of the 3DUNET to be narrower, since it has less segmented keratocytes that the segmented image by the conventional method, however the curve has the inverse behaviour.

In this thesis, it is important to note that neither glare nor contrast sensitivity were evaluated. These aspects should be subjects of future research. Nevertheless, a qualitative visual assessment of Figure 3.5a suggests low glare due to the progressive decay of the curve (reaching one-quarter of the intensity in the peak), which is expected in healthy corneas. The high values in the region close to the peak (0.06º-0.33º) also indicate a reasonable contrast sensitivity.

The characteristics of this dataset present an opportunity for additional investigation. Exploring additional datasets with similar characteristics can help determine which method aligns more closely with the expected results and better reflects the actual anatomical features of the cornea.

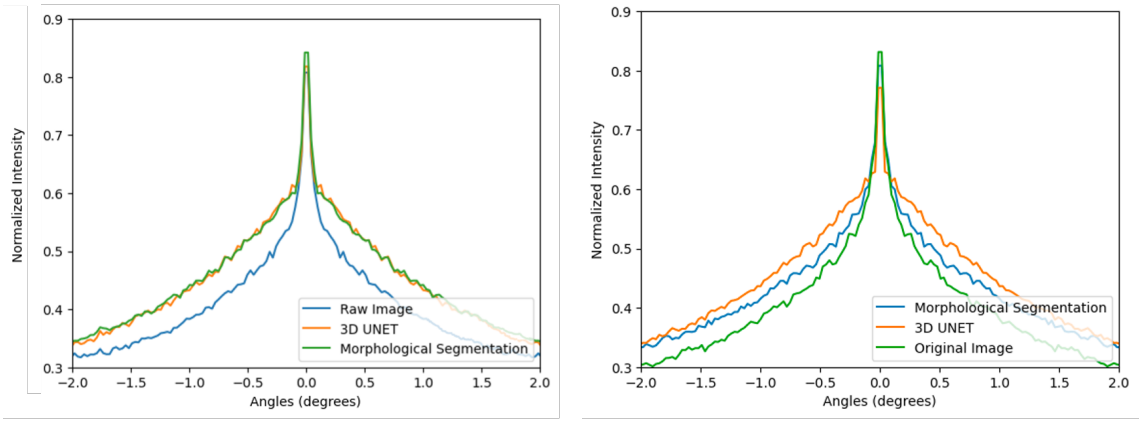

(a) PSF of non-fixed cornea 3C

(b) PSF of fixed cornea

Figure 3.6: Differences between PSF curves of fixed cornea and non-fixed cornea. The y-axis values were calculated using a log scale and normalised.

In summary, all the PSF curves exhibited the expected behaviour of a healthy cornea. The sharp and intense central peaks indicate that light is focused accurately onto the centre regions (potentially the retina), contributing to clear vision. The well-defined and symmetric distribution suggests that light is evenly spread, indicating low-level optical aberrations.

Strehl ratio

The Strehl Ratio is an interesting parameter to determine in the analysis, even though it just acts as a primary indicator of the level of aberrations of the cornea.

Figure 3.7a closely examines the PSF curve's peak, emphasizing the differences in the maximum values of each curve. Although these differences exist, they are relatively subtle (0.03 between both methods), indicating that the corneal aberrations, while present, may not substantially distort the PSF. Figure 3.7b presents the calculated Strehl Ratio values for the various corneas under evaluation. The first consideration of this image is the high values of the Strehl ratio obtained for both methods, over 0.75, an expected value for healthy corneas. Notably, the conventional segmentation method generates a higher Strehl Ratio than the 3DUNET method for all images, with differences typically falling from 1% to 14%. However, whether these differences are considered negligible requires a more careful analysis of the aberrations present in the system. In diseased corneas, the scattering level will be higher, so the Strehl Ratio is expected to be smaller due to the broadening of the PSF.

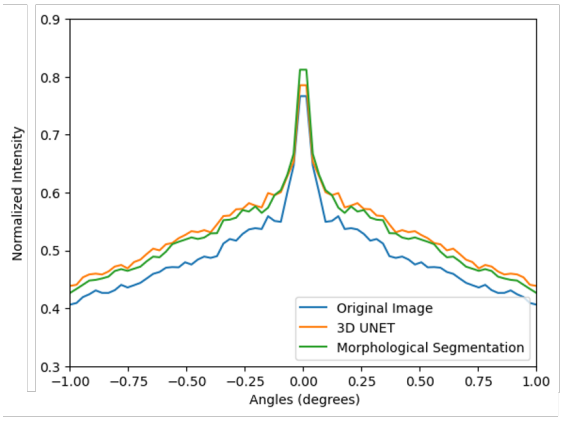

(a) Zoom of PSF curve of Non-Fixed Cornea 1A

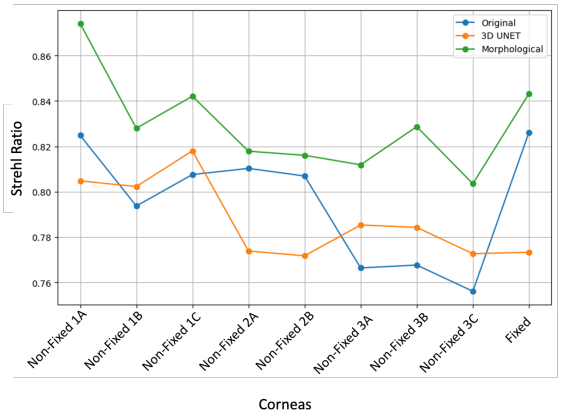

(b) Strehl Ration for the diverse datasets available

Figure 3.7: Strehl Ratio

Therefore, the Strehl Ratio provides a valuable numerical value that summarizes overall optical quality but does not specify the nature or type of aberrations present. It can be helpful to the early estimation of the state of the cornea and should be regarded as just one piece of the puzzle in assessing corneal optics.

Visual acuity

Visual acuity represents one of the most essential aspects of visual function as it assesses the quality of vision. Figure 3.8 shows the values obtained for both methods and the original image. Since the case of the study is healthy corneas, the presentation of high visual acuity values is entirely expected and representative of the low scattering that occurs in

these types of cornea. The higher the area inside the (-0.02º-0.02º) range, the higher the intensity of light going through the centre, which indicates good vision quality.

It is noteworthy that, despite the differences between the two segmentation methods, they yield similar estimations of the level of vision quality. Visual acuity is valuable for assessing the current state of the cornea and can also be a useful metric for monitoring changes that occur during processes such as deswelling. As Figure 3.8 highlights, there are changes in visual acuity as part of the deswelling process.

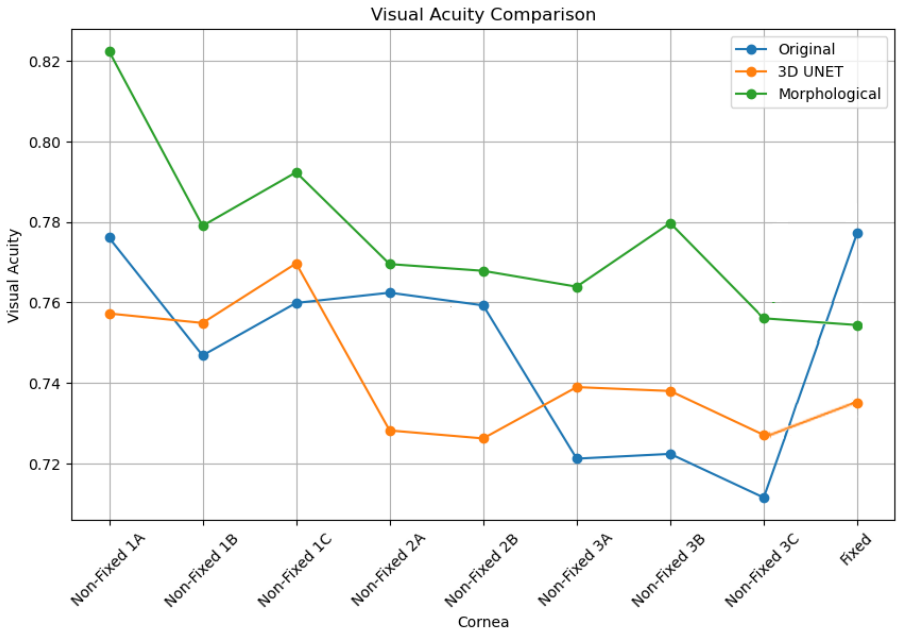

Figure 3.8: Visual Acuity of available corneas

Conclusion

In a global context of increasing cases of cornea disease, early detection, objective diagnosis, and standardised procedures to monitor patients are essential to prevent severe advanced cases of pathologies. The increasing use and efficiency of artificial intelligence models in medical imaging represent an opportunity to create robust AI-based models to help in disease detection and treatment.

This thesis paves the way for creating a complete model that detects relevant objects in images obtained through standard ophthalmological examinations and subsequently evaluates these objects' impact on the cornea's clinical status. The first phase of this thesis addresses the potential of a deep learning architecture in the segmentation of keratocytes, cells present in the cornea that influence the cornea's transparency, using high-resolution OCT data, similar to the standard low-resolution examination technique in clinical routine. This method consistently outperforms the accuracy and processing time of conventional techniques. The possibility of more training sessions with more exotic datasets (pathological corneas) shows this method's generalisation capability and high potential to efficiently segment the object inside the cornea without needing consistent verification of the segmentation quality, improving the autonomy of potential medical tools.

The second phase evaluates the distribution and structure of segmented keratocytes and their influence on foundational metrics in the analysis of the eye as a physical system, such as Point Spread Function (PSF), Strehl ratio, and visual acuity, to characterise the clinical status of the cornea. It also allowed comparing the differences between the two segmentations with a Fourier analysis. In general, the two methods don't produce major differences in the metrics having similar values for all datasets available.

The limitation to healthy corneas facilitated the creation, evaluation and optimisation of the workflow as it not only reduced the computational cost of the workflow due to lower complexity but also allowed the results to be compared with theoretical values expected for healthy corneas.

Future research should prioritise four main points: the study of pathological conditions to expand the understanding of the impact of these diseases on the chosen analysis parameters; the study of the high-angle scattering in the cornea to complement the knowledge of the low-angle regime to develop a complete model of the scattering in the cornea;

transfer the model to high resolution in vivo images and then low-resolution clinical data and the translation of these metrics into user-friendly clinical tools for corneal transparency characterisation. These four points can collectively contribute to creating a robust model to detect and diagnose the cornea state, addressing a critical need in the field of ophthalmology.

References

[1] D. Atchison, E. Markwell, S. Kasthurirangan, J. Pope, G. Smith, and P. Swann. Age-related changes in optical and biometric characteristics of emmetropic eyes. *Journal of vision*, 8:29.1–20, 04 2008.

[2] R. Bocheux. *Caractérisation objective et quantitative de la transparence cornéenne par OCT plein champ et microscopie holographique*. Theses, Université Paris Saclay (COmUE), Sept. 2019.

[3] M. A. Choma, M. V. Sarunic, C. Yang, and J. A. Izatt. Sensitivity advantage of swept source and fourier domain optical coherence tomography. *Opt. Express*, 11(18):2183–2189, Sep 2003.

[4] Ö. Çiçek, A. Abdulkadir, S. S. Lienkamp, T. Brox, and O. Ronneberger. 3d u-net: Learning dense volumetric segmentation from sparse annotation. In S. Ourselin, L. Joskowicz, M. R. Sabuncu, G. Unal, and W. Wells, editors, *Medical Image Computing and Computer-Assisted Intervention – MICCAI 2016*, pages 424–432, Cham, 2016. Springer International Publishing.

[5] Devskrol. Digital image processing - morphological operations, December 2021. [Online; accessed 29-july-2023.

[6] W. Drexler, M. Liu, A. Kumar, T. Kamali, A. Unterhuber, and R. Leitgeb. Optical coherence tomography today: Speed, contrast, and multimodality. *Journal of biomedical optics*, 19:71412, 07 2014.

[7] D. Gatinel. Topographie cornéenne : cartes de courbure, 2014.

[8] D. Gatinel. La pupille de l'oeil, 2015.

[9] A. Gullstrand. *How I found the mechanism of intracapsular accommodation*. Elsevier, Amsterdam, 1967.

[10] X. Guo and U. Riebel. Theoretical direct correlation function for two-dimensional fluids of monodisperse hard spheres. *The Journal of Chemical Physics*, 125(14):144504, 10 2006.

[11] S. Khanal. Relationships between pixels: Neighbours and connectivity, Publication date unavailable. Medium.

[12] C. Kniestedt and R. L. Stamper. Visual acuity and its measurement. *Ophthalmology clinics of North America*, 16(2):155—70, v, June 2003.

[13] D. M. Maurice. The structure and transparency of the cornea. *The Journal of Physiology*, 136(2):263–286, 1957.

[14] K. M. Meek and C. Knupp. Corneal structure and transparency. *Progress in Retinal and Eye Research*, 49:1–16, 2015.

[15] S. Patel and L. Tutchenko. The refractive index of the human cornea: A review. *Contact Lens and Anterior Eye*, 42(5):575–580, 2019.

[16] J. K. Percus and G. J. Yevick. Analysis of classical statistical mechanics by means of collective coordinates. *Phys. Rev.*, 110:1–13, Apr 1958.

[17] V. K. Rajput. Robustness of different loss functions and their impact on networks learning capability. *ArXiv*, abs/2110.08322, 2021.

[18] K. Reda, V. Mateevitsi, and C. Offord. A human-computer collaborative workflow for the acquisition and analysis of terrestrial insect movement in behavioral field studies. *EURASIP Journal on Image and Video Processing*, 2013:48, 12 2013.

[19] R. Schiffer and K. O. Thielheim. Light scattering by dielectric needles and disks. *Journal of Applied Physics*, 50:2476–2483, 1979.

[20] H. Strasburger, I. Rentschler, and M. Jüttner. Peripheral vision and pattern recognition: A review. *Journal of vision*, 11:13, 05 2011.

[21] A. Tezel, J. S. Schuman, and G. Wollstein. *Fundamentals of OCT for Glaucoma*, pages 1–9. Springer International Publishing, Cham, 2020.

[22] A. V. van den Berg. Visual acuity, 2010. Accessed: September 20, 2023.

[23] M. Vilbert. *Diagnostic optique in vivo de la transparence cornéenne par tomographie par cohérence optique (OCT)*. Theses, Institut Polytechnique de Paris, Oct. 2022.

[24] Wikipedia contributors. Optical coherence tomography — Wikipedia, the free encyclopedia, 2023. [Online; accessed 27-July-2023].

[25] Wikipedia contributors. Otsu's method — Wikipedia, the free encyclopedia, Year of the latest revision. [Online; accessed 29-august-2023].

[26] M. Wojtkowski, R. Leitgeb, A. Kowalczyk, T. Bajraszewski, and A. Fercher. In vivo human retinal imaging by fourier domain optical coherence tomography. *Journal of biomedical optics*, 7:457–63, 08 2002.

[27] J. G. F. Wolfgang Drexler. *Optical Coherence Tomography*. International series of monographs on physics. Springer Cham, 2015.